

AD-A207 665

RAYLEIGH LIDAR OBSERVATIONS OF GRAVITY WAVE ACTIVITY IN THE UPPER STRATOS (U) ILLINOIS UNIV AT URBANA DEPT OF ELECTRICAL AND COMPUTER ENGIN M S MILLER ET AL

171

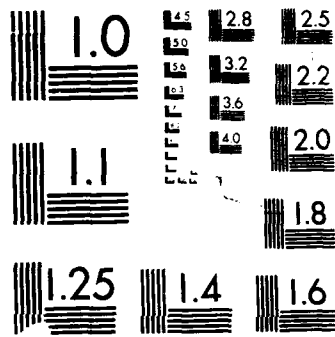
UNCLASSIFIED

DEC 87 SCIENTIFIC-1 AFGL-TR-88-0270

F/G 4/2

NL

END
10 MAR 88
DTIC



4

AFGL-TR-88-0270

AD-A207 665

Rayleigh Lidar Observations of
Gravity Wave Activity in the Upper
Stratosphere at Urbana, Illinois

M. S. Miller
C.S. Gardner
C.H. Liu

University of Illinois
Department of Electrical and
Computer Engineering
College of Engineering
Urbana, IL 61801

December 1987

DTIC
ELECTE
MAY 15 1989
S D D

Scientific Report No. 1

APPROVED FOR PUBLIC RELEASE; DISTRIBUTION UNLIMITED

AIR FORCE GEOPHYSICS LABORATORY
AIR FORCE SYSTEMS COMMAND
UNITED STATES AIR FORCE
HANSOM AIR FORCE BASE, MASSACHUSETTS 01731-5000

89 5 15 031

"This technical report has been reviewed and is approved for publication"



ROSS T. MCNUTT
Contract Manager



JOHN E. RASMUSSEN
Branch Chief

FOR THE COMMANDER



ROBERT A. SKRIVANEK
Division Director

This report has been reviewed by the ESD Public Affairs Office (PA) and is releasable to the National Technical Information Service (NTIS).

Qualified requestors may obtain additional copies from the Defense Technical Information Center. All others should apply to the National Technical Information Service.

If your address has changed, or if you wish to be removed from the mailing list, or if the addressee is no longer employed by your organization, please notify AFGL/DAA, Hanscom AFB, MA 01731-5000. This will assist us in maintaining a current mailing list.

Do not return copies of this report unless contractual obligations or notices on a specific document requires that it be returned.

Unclassified

SECURITY CLASSIFICATION OF THIS PAGE

REPORT DOCUMENTATION PAGE				
1a REPORT SECURITY CLASSIFICATION Unclassified		1b. RESTRICTIVE MARKINGS		
2a SECURITY CLASSIFICATION AUTHORITY		3. DISTRIBUTION/AVAILABILITY OF REPORT Approved for public release; Distribution unlimited		
2b DECLASSIFICATION/DOWNGRADING SCHEDULE				
4. PERFORMING ORGANIZATION REPORT NUMBER(S)		5. MONITORING ORGANIZATION REPORT NUMBER(S) AFGL-TR-88-0270		
5a NAME OF PERFORMING ORGANIZATION University of Illinois Dept of Electrical & Computer Engr, College of Engr	5b OFFICE SYMBOL (If applicable)	7a NAME OF MONITORING ORGANIZATION Air Force Geophysics Laboratory		
6c ADDRESS (City, State, and ZIP Code) Urbana, Illinois 61801		7b ADDRESS (City, State, and ZIP Code) Hanscom AFB Massachusetts 01731-5000		
8a. NAME OF FUNDING/SPONSORING ORGANIZATION	8b. OFFICE SYMBOL (If applicable)	9 PROCUREMENT INSTRUMENT IDENTIFICATION NUMBER MIPR FY7121-87-03292 (Project Order GLH-7-6029)		
8c. ADDRESS (City, State, and ZIP Code)		10 SOURCE OF FUNDING NUMBERS		
		PROGRAM ELEMENT NO. 62101F	PROJECT NO 7670	TASK NO 16
11. TITLE (Include Security Classification) Rayleigh Lidar Observations of Gravity Wave Activity in the Upper Stratosphere at Urbana, Illinois				
12. PERSONAL AUTHOR(S) M. S. Miller, C.S. Gardner, C.H. Liu				
13a. TYPE OF REPORT Scientific Report #1	13b. TIME COVERED FROM TO	14. DATE OF REPORT (Year, Month, Day) 1987 December	15. PAGE COUNT 64	
16. SUPPLEMENTARY NOTATION				
17 COSATI CODES		18 SUBJECT TERMS (Continue on reverse if necessary and identify by block number)		
FIELD	GROUP	SUB-GROUP		
			Lidar measurements Atmospheric dynamics	
			Rayleigh lidar measurements	
			Gravity waves	
19 ABSTRACT (Continue on reverse if necessary and identify by block number)				
<p>→ During 13 night of Rayleigh lidar measurements at Urbana, IL in 1984 - 86, thirty-six quasi-monochromatic gravity waves were observed in the 35 to 50 km altitude region of the stratosphere. The characteristics of the waves are compared with other lidar and radar measurements of gravity waves and with theoretical models of wave saturation and dissipation phenomena. The measured vertical wavelengths (λ_z) ranged from 2 to 11.5 km and the measured vertical phase velocities (c_z) ranged from 10 to 85 cm s⁻¹. The vertical wavelengths and vertical phase velocities were used to infer observed wave periods (T_{ob})</p>				
20 DISTRIBUTION/AVAILABILITY OF ABSTRACT <input type="checkbox"/> UNCLASSIFIED/UNLIMITED <input type="checkbox"/> SAME AS RPT <input type="checkbox"/> OTIC USERS		21 ABSTRACT SECURITY CLASSIFICATION Unclassified		
22a NAME OF RESPONSIBLE INDIVIDUAL Ross McNutt		22b TELEPHONE (Include Area Code) (617) 377-8756	22c OFFICE SYMBOL AFGL/LID	

DD FORM 1473, 84 MAR

83 APR edition may be used until exhausted
All other editions are obsoleteSECURITY CLASSIFICATION OF THIS PAGE
Unclassified

which ranged from 100 to 1000 min and horizontal wavelengths (λ_x) which ranged from 70 to 2000 km. However, there may be errors in the inferred values of the horizontal wavelengths because they were calculated by assuming that the observed period equals the intrinsic period. Dominant wave activity was found at vertical wavelengths between 2-4 km and 7-10 km. No significant seasonal variations were evident in the observed parameters. Vertical and horizontal wavelengths showed a clear tendency to increase with T_{ob} , which is consistent with recent sodium lidar studies of quasi-monochromatic waves near the mesopause. An average amplitude growth length of 20.9 km for rms wind perturbations was estimated from the data. Kinetic energy density associated with the waves decreased with height, suggesting that waves in this altitude region were subject to dissipation or saturation effects.



Accession For	
NTIS CRA&I	<input checked="" type="checkbox"/>
DTIC TAB	<input type="checkbox"/>
Unannounced	<input type="checkbox"/>
Justification	
By _____	
Distribution /	
Availability Codes	
Dist	Avail and/or Special
A-1	

1. INTRODUCTION

It is now widely recognized that atmospheric gravity waves play a major role in determining the large-scale circulation and structure of the middle atmosphere. Observational studies of gravity-wave activity have focused on measurements of quasi-monochromatic wave parameters and characterization of the continuous gravity-wave spectra in order to quantify wave saturation effects and the variability of wave activity with altitude, season and location [Fritts, 1984]. Analyses of the vertical wave number spectra of atmospheric wind fluctuations suggest the existence of an invariant spectral shape, which is predicted as a consequence of the saturation of vertically propagating gravity waves [Dewan and Good, 1986; Smith et al., 1987]. Radar and lidar are the predominant remote sensing techniques used to study gravity waves in the middle atmosphere. Radars have been successfully used to measure the vertical wave number and temporal frequency spectra of gravity waves [e.g., Smith et al., 1985; Balsley and Carter, 1982]. Statistical studies of the variability of wave motions and wave characteristics as a function of altitude and time have been accomplished in the 60-110 km altitude region using several MF radar techniques [Meek et al., 1985; Vincent and Fritts, 1987; Ebel et al., 1987; Manson and Meek, 1988; Reid and Vincent, 1987].

The feasibility of studying atmospheric dynamics with lidar techniques based on resonant backscatter from sodium atoms and Rayleigh backscatter from the atmosphere is well established. Lidar studies of gravity wave activity generally concentrate on observations of quasi-monochromatic events, since wave perturbations usually appear as individual events in lidar profiles. The University of Illinois at Urbana-Champaign (UIUC) sodium lidar has been used to observe the spatial and temporal variations in the

sodium layer in the 80-105 km altitude region and to study the propagation of gravity waves near the mesopause [Rowlett et al., 1978; Richter et al., 1981; Shelton et al., 1980; Gardner et al., 1986]. The parameters of monochromatic gravity waves can be inferred from sodium density perturbations [Gardner and Shelton, 1985] and used to infer wave saturation and dissipation effects [Gardner and Voelz, 1985]. An extensive characterization of monochromatic gravity waves appearing in the sodium layer above Urbana, Illinois was published recently by Gardner and Voelz [1987].

The altitude region from 25-60 km is generally inaccessible with existing MST radar and has not been studied extensively. The lack of observational data in this region provides the scientific motivation for Rayleigh lidar studies of atmospheric dynamics. The observation altitudes for Rayleigh scatter are not limited to regions containing specific atmospheric constituents, as with sodium lidar and other resonance fluorescence lidar techniques. Rayleigh lidar measurements are impeded only by the presence of aerosols in the atmosphere and by system noise. Rayleigh systems have been successfully used to measure atmospheric density and temperature in the 30-80 km altitude region as well as to study gravity wave activity [Hauchecorne and Chanin, 1980; Chanin and Hauchecorne, 1981; Shibata et al., 1986a].

In this paper we investigate the feasibility of using Rayleigh lidars to study gravity-wave characteristics in the upper stratosphere. We present the results of 13 nights of Rayleigh lidar measurements at Urbana, Illinois ($40^{\circ} 10' \text{ N}$, $88^{\circ} 10' \text{ W}$), during which 36 quasi-monochromatic gravity waves were identified and characterized. The lidar used in this study was the UIUC sodium lidar which is a relatively low-performance system when compared to state-of-the-art Rayleigh lidars. However, the temporal and spatial resolutions are sufficient to observe monochromatic waves and to measure the critical wave parameters. In Section 2, the theoretical expressions used to characterize the atmospheric density response to monochromatic gravity wave perturbations are derived. The data-processing technique used to infer the wave spectrum and horizontal wind perturbations

from the measured density perturbations is discussed in Section 3. Representative examples of observed wave events are illustrated in Section 4. Seasonal variations of the measured gravity-wave parameters and the relationships between the parameters are presented and compared to previous radar and lidar observations in Sections 5 and 6. Altitude variations of rms wind perturbations are examined in Section 7. Rayleigh lidar performance and data processing tradeoffs are discussed in the Appendix.

2. ATMOSPHERIC DENSITY RESPONSE

The atmospheric density response to gravity-wave motions is governed by the continuity equation. By neglecting diffusion, Gardner and Shelton [1985] have shown that the density response can be written in the form

$$\rho(z,t) = e^{-\phi} \rho_0(z - \theta_z) \quad (1)$$

where

$\rho(z,t)$ = atmospheric density at altitude z and time t ;

$\rho_0(z)$ = steady-state atmospheric density in the absence of wind perturbations and

$$\phi(\underline{r},t) \approx \int_{-\infty}^t \nabla \cdot \underline{v} \, d\tau \quad (2)$$

$$\theta_z(\underline{r},t) \approx \int_{-\infty}^t v_z \, d\tau \quad (3)$$

$\underline{r} = x \hat{x} + z \hat{z}$ is the position vector where x is the horizontal coordinate and z is the vertical coordinate. The wind vector is defined as

$$\underline{v} = v_x \hat{x} + v_z \hat{z} \quad (4)$$

For monochromatic gravity-wave perturbations, the polarization and dispersion relations can be used to show that [Gardner and Voelz, 1987]

$$\theta_z = \gamma H \phi \quad (5)$$

under the condition where $\lambda_z \ll 4\pi H$ and $\omega \ll N$, where γ is the ratio of specific heats, H is the atmospheric scale height, $N = [(\gamma-1)g/\gamma H]^{1/2}$ is the Brunt-Väisälä frequency, g is the gravitational acceleration, λ_z is the vertical wavelength of the wave and ω is the wave frequency. The influence of earth's rotation on gravity waves is also neglected. In an isothermal atmosphere the steady-state density decreases exponentially with altitude ($\rho_0 \sim e^{-z/H}$) so that, by substituting Eq. (5) into Eq. (1) we obtain for gravity-wave perturbations

$$\rho(z,t) = e^{(\gamma-1)\phi} \rho_0(z) . \quad (6)$$

For our purposes it is most convenient to work with the natural logarithm of the relative density perturbations

$$r(z,t) = \ln(\rho/\rho_0) = (\gamma-1)\phi = \left(\frac{\gamma-1}{\gamma H}\right) \theta_z . \quad (7)$$

The gravity-wave polarization and dispersion relations can be used to relate the vertical wave number spectra and mean-square values of ϕ and θ_z to the power spectrum $E_X(k_z)$ and mean-square value of the horizontal winds $\langle v_x^2 \rangle$ [Miller et al., 1987]

$$E_X(k_z) = (\gamma H N)^2 E_\phi(k_z) = N^2 E_{\theta_z}(k_z) \quad (8)$$

$$\langle v_x^2 \rangle = (\gamma H N)^2 \langle \phi^2 \rangle = N^2 \langle \theta_z^2 \rangle. \quad (9)$$

As a consequence of Eqs. (7) - (9), the gravity-wave spectrum and mean-square wind velocity can be expressed in terms of the Fourier transform and mean-square value of $r(z,t)$ [Miller et al., 1987]

$$E_x(k_z) = \left(\frac{\gamma H N}{\gamma - 1} \right)^2 \frac{\langle |R(k_z)|^2 \rangle}{L} \quad (10)$$

$$\langle v_x^2 \rangle = \left(\frac{\gamma H N}{\gamma - 1} \right)^2 \langle r^2(z,t) \rangle \quad (11)$$

where

$$R(k_z) = \int_{z_c - L/2}^{z_c + L/2} r(z,t) e^{ik_z z} dz. \quad (12)$$

L is the altitude range of observations and z_c is the altitude at the center of the observation interval.

For the case of low-frequency monochromatic waves, exact solutions for ϕ and θ_z were derived by Gardner and Shelton [1985].

$$\phi = \ln \left[1 + \frac{A e^{\beta z}}{\gamma - 1} \cos(\omega t - \underline{k} \cdot \underline{r}) \right] \quad (13)$$

$$\theta_z = \gamma H \ln \left[1 + \frac{A e^{\beta z}}{\gamma - 1} \cos(\omega t - \underline{k} \cdot \underline{r}) \right] \quad (14)$$

where

$Ae^{\beta z}$ = wave amplitude

β = amplitude growth factor (m^{-1})

ω = wave frequency (s^{-1})

$\underline{k} = k_x \hat{x} + k_z \hat{z}$ = wave number vector (m^{-1})

k_x = horizontal wave number (m^{-1})

k_z = vertical wave number (m^{-1}).

The corresponding vertical and horizontal winds generated by an unsaturated gravity wave are given by [Hines, 1960]

$$v_z \approx -\frac{\gamma H N}{\gamma - 1} \frac{\lambda_z}{\lambda_x} A e^{\beta z} \sin(\omega t - \underline{k} \cdot \underline{r}) \quad (15)$$

$$v_x \approx \frac{\gamma H N}{\gamma - 1} A e^{\beta z} \sin(\omega t - \underline{k} \cdot \underline{r}) \quad (16)$$

The vertical and horizontal wavelengths are, respectively, λ_z and λ_x . The linear density perturbation is obtained by substituting Eq. (13) into (7) and noting that the wave amplitude is small (<10%)

$$r(z,t) = (\gamma - 1) \ln \left[1 + \frac{A e^{\beta z}}{\gamma - 1} \cos(\omega t - \underline{k} \cdot \underline{r}) \right] \approx A e^{\beta z} \cos(\omega t - \underline{k} \cdot \underline{r}) \quad (17)$$

Because the density perturbation, $r(z,t)$, and horizontal velocity perturbation, v_x , are proportional and 90° out of phase, their respective power spectra are proportional, and Eqs. (10) and (11) result.

The kinetic energy per unit mass of a quasi-monochromatic wave is defined as

$$KE(\underline{k}, \omega) = \frac{1}{2} |v_x|^2 + \frac{1}{2} |v_z|^2 \quad (18)$$

where in this case v_x and v_z are the complex amplitudes of the horizontal and vertical wind velocities. For low-frequency waves $\lambda_z \ll \lambda_x$, so that

$$KE(\underline{k}, \omega) \approx \frac{1}{2} |v_x|^2 = \frac{1}{2} \left(\frac{\gamma H N}{\gamma - 1} \right)^2 (Ae^{\beta z})^2. \quad (19)$$

The presence of quasi-monochromatic waves in the lidar profiles of $r(z, t)$ can be determined by examining the spectrum. The spectral signature for a wave is computed using Eqs. (10), (12), and (17) [Miller et al., 1987].

$$E_x(k) = \frac{1}{L} \left(\frac{\gamma H N}{\gamma - 1} \right)^2 (Ae^{\beta z_c})^2 \left[\frac{\cosh(\beta L) - 1}{2((k - k_z)^2 + \beta^2)} + \frac{\sin^2(L(k - k_z)/2)}{((k - k_z)^2 + \beta^2)} \right] \quad (20)$$

Equation (20) is plotted in Figure 1 for $\lambda_z = 7.5$ km, $Ae^{\beta z} = 0.01$, $L = 15$ km and several values of β . The spectral peak occurs at the spatial frequency λ_z^{-1} , and the magnitude in m^3/s^2 is

$$E_x(k = k_z) = \frac{L}{8} \left(\frac{\gamma H N}{\gamma - 1} \right)^2 (Ae^{\beta z_c})^2 \left[\frac{\sinh(\beta L/2)}{(\beta L/2)} \right]^2 = \frac{L}{4} KE(z_c) \left[\frac{\sinh(\beta L/2)}{(\beta L/2)} \right]^2 \quad (21)$$

where $KE(z_c)$ (Eq.(19)) is the wave kinetic energy per unit mass at altitude z_c , the center of the observation interval. The vertical wavelength of a monochromatic wave can be determined by measuring the spatial frequency of the spectral peak. For most of the data reported here, $\beta L \leq 1$, so that the square of the bracketed form in Eq. (21) is approximately 1. Thus the wave amplitude and kinetic energy at altitude z_c can be computed from the

magnitude of the spectral peak using Eq. (21). The vertical phase velocity (c_z) of the wave is measured directly from the density perturbation profiles.

3. EXPERIMENTAL DATA

The data used in this study were obtained at Urbana, Illinois, by using the Rayleigh scatter photocounts from lidar profiles measured during 1984-86 with the UIUC sodium lidar system. The UIUC lidar utilizes a flashlamp-pumped dye laser tuned to the sodium resonance line at 589 nm. The operational characteristics of the UIUC lidar system are described in Gardner et al. [1986]. The parameters of the lidar are listed in Table 1.

The UIUC lidar counts backscattered photons from a single laser shot in discrete time intervals that correspond to range bins. The data consist of 100 second photocount profiles with a range resolution of 150 m obtained by integrating backscattered photocounts from 750 laser shots. Absolute density was computed by referencing photocounts near 25 km altitude to the atmospheric density specified in the U.S. Standard Atmosphere.

Photocount profiles can be contaminated by Mie scattering caused by the presence of atmospheric aerosols in the propagation path of the laser beam. Rayleigh scattering is caused by air molecules and by small aerosols whose the radii satisfy the condition $r \leq 0.03\lambda$. Mie scattering is caused by larger aerosols and particulates such as volcanic ash, meteoric dust and water droplets in clouds [Cerny and Sechrist, 1980]. Techniques have been developed to detect the presence of aerosols and determine regions of pure Rayleigh scattering. These techniques utilize two lasers operating at different frequencies to exploit the different wavelength dependence of Mie (λ^{-1}) and Rayleigh (λ^{-4}) scattering cross sections. Typically, these studies show no aerosols above 25-30 km [Chanin and Hauchecorne, 1981; Philbrick et al. 1987]. In the UIUC lidar profiles, the lowest usable Rayleigh scatter altitude is also limited by photomultiplier (PMT) blanking which is employed to prevent receiver overload from strong backscatter returns at low altitudes. For the measurements reported here, the PMT gain was switched to maximum at an altitude

near 30 km. Because the Rayleigh signal decreases rapidly with altitude, the maximum usable altitude is dictated by system noise.

Rayleigh scatter photocount data can be readily converted to density perturbation measurements because the range-scaled signal photocounts are proportional to atmospheric density. Atmospheric density is estimated from measured photocount data by range scaling the signal photocounts and then multiplying the result by a scaling constant ξ ,

$$\rho(z,t) = \xi z^2 [N(z,t) - N_B(t)] \quad (22)$$

where $N(z,t)$ is the photocount at altitude z measured at observation time t and $N_B(t)$ is the background photocount per range bin. The density perturbation at altitude z and time t is given by (Eq. (7))

$$r(z,t) = \ln(\rho/\rho_0) \simeq \frac{\rho(z,t)}{\rho_0(z)} - 1 \quad (23)$$

The second equality holds when the density perturbations are small, which is the case for gravity wave effects. The mean atmospheric density ρ_0 is estimated by averaging the density profiles over the whole observation period

$$\rho_0(z) \simeq \frac{1}{T_0} \int_{t_0}^{t_0+T_0} \rho(z,t) dt = \frac{1}{T_0} \int_{t_0}^{t_0+T_0} \xi^2 z^2 [N(z,t) - N_B(t)] dt \quad (24)$$

where T_0 is the duration of the observation period (typically 6 to 10 hrs).

The estimated vertical wave number spectrum obtained from the Rayleigh photocount data contains a signal component $E_X(k_z)$ contaminated by shot noise. While the vertical resolution of lidar profiles is fundamentally governed by the width of the receiver range-gate, the practical resolution limits are determined by shot noise, which is a function of

laser power, receiver telescope area, integration time and observation range. The expected vertical wave number spectrum obtained by scaling the spatial power spectrum of the density perturbations according to Eq. (10) will have the form (see Appendix)

$$\frac{1}{L} \left(\frac{\gamma H N}{\gamma - 1} \right)^2 \langle |R(k_z)|^2 \rangle = E_x(k_z) + \frac{1}{L} \left(\frac{\gamma H N}{\gamma - 1} \right)^2 \frac{H^2}{N_T} \left(1 + \frac{L-H}{z_0} \right)^2 e^{L/H} \quad (25)$$

where N_T is the total signal photocount within the observation range ($z_0, z_0 + L$) comprising a single lidar profile. The first term on the right side of Eq. (25) is the vertical wave number spectrum while the second term is the shot noise component. The linear saturation theory predicts that the vertical wave number spectrum of horizontal wind perturbations has approximately a k_z^{-3} dependence [Dewan and Good, 1986; Smith et al., 1987]

$$E_x(k_z) \propto \frac{N^2}{2k_z^3} \quad (26)$$

The proportionality constant relating the right-hand-side of Eq. (26) to $E_x(k_z)$ is on the order of unity. In principle, the theory of Dewan and Good [1986] allows exponents other than exactly -3. However, much of the existing experimental data indicate that the k_z exponent is very near -3 and this value will be assumed in the subsequent analysis. Equation (26) must be greater than the shot noise floor in order to reliably measure wave parameters. Shorter wavelengths can only be observed by decreasing the shot noise contamination. The shot noise floor is reduced by increasing N_T , the total signal photocount in a profile, or by reducing the altitude range of observations, L . However, the use of longer integration periods needed to increase N_T reduces the temporal resolution and may average out wave events with shorter periods. Decreasing the altitude range of

observation will exclude longer wavelength events. Equation (25) is derived in the Appendix and is used to predict the spatial resolution of Rayleigh lidar measurements based on the model spectrum.

The procedure used to process Rayleigh photocount data is similar to the method that has been used effectively to process the UIUC sodium lidar data [Rowlett et al., 1978]. Photocount data are integrated over adjacent observation times to reduce shot noise levels. Density perturbation profiles are then calculated from the integrated photocount profiles. The vertical wave number spectrum of each profile is obtained by scaling the spatial power spectrum of the density perturbation profile according to Eq. (10). Vertical wavelength (λ_z) and wave kinetic energy ($KE(k_c)$) are measured from the vertical wave number spectrum. Each density perturbation profile is spatially low-pass filtered in the Fourier domain to reduce high frequency shot noise. Vertical phase velocity (c_z) is then measured by observing the phase progression of the waves in the spatially filtered density perturbation profiles. Other characteristics of discrete wave events such as observed period are inferred from the measured parameters.

4. GRAVITY WAVE CASE STUDIES

To illustrate the analysis technique, we now discuss several wave events observed at Urbana, Illinois with the UIUC lidar system. Because the Rayleigh signal levels for the UIUC Na lidar are relatively weak compared to state-of-the-art Rayleigh lidars, the photocount profiles were integrated for 60 minutes to reduce signal shot noise. To reduce computation time the vertical resolution was reduced from 150 m to 300 m by summing the counts in each pair of consecutive range bins. The 1-hour profiles were then averaged to obtain an estimate of the mean atmospheric density profile for the night. Finally, the perturbation about the mean density was then computed for each 60-minute profile. The altitude range of interest was usually restricted to 35-50 km.

The spatial power spectrum of each density perturbation profile was computed by calculating the magnitude squared of the discrete Fourier transform. A raised cosine tapering function was used to window the spatial profile in order to control sidelobe effects in the power spectrum. The vertical wave number spectrum of the horizontal winds associated with the gravity waves was then obtained by scaling this spatial power spectrum by $[\gamma H N / (\gamma - 1)]^2$ (Eq. (10)). The spatial power spectra obtained during the evening's observations were averaged to reduce the variance of the spectral estimate. The average vertical wave number spectrum for 13 August 1984 is shown in Figure 2. Energy density $E_x(k_z)$ is plotted versus vertical wave number $k_z/2\pi$ from L^{-1} to the Nyquist frequency $(2\Delta z)^{-1}$ where $L = 15$ km is the observation range and $\Delta z = 300$ m is the range bin length. The dashed line is the estimated shot noise floor. A spectral peak near $k_z/2\pi = 1.3 \times 10^{-4}$ cyc/m ($\lambda_z = 7.7$ km) dominates the power spectrum. The signal-to-noise ratio at this peak is almost 7 dB.

The density perturbation profiles measured on 13 August were spatially filtered with a cutoff wave number of 2×10^{-4} cyc/m (1 cyc/5 km). Wave-like structures are clearly present in the spatially filtered profiles. In particular, the six consecutive profiles corresponding to the observation interval 21:00 to 03:00 (LST) shown in Figure 3 exhibit a wave structure with downward phase progression. When this wave was strongest, the amplitude inferred from the spatial power spectrum was 2.83%. A vertical phase velocity of 0.32 m/s is calculated from the slope of the phase progression. Smaller vertical wavelengths were also observed in the Urbana data. Figure 4 shows the filtered profiles measured on 29 February - 1 March 1984. The spatial cutoff wavelength is 1.8 km. A vertical wavelength near 2.4 km and 0.25 m/s downward phase progression is evident in the data.

5. SEASONAL VARIATION OF GRAVITY WAVE PARAMETERS

Wave-like structures were observed in almost all density perturbation profiles examined for this study. Coherent downward phase progression was identified in two or more consecutive profiles at least once during each of the 13 observation nights. Previous Rayleigh lidar observations in the 30-70 km altitude range at Haute Provence indicated that wave structures are almost always present in the density profiles for 5 to 60 minute integration periods [Chanin and Hauchecorne, 1981]. For the Urbana data, a total of 36 monochromatic waves were observed during the 13 nights. Figure 5 shows the average vertical wave number spectrum for the 1984 Urbana data.

Vertical wavelength (λ_z), vertical phase velocity (c_z), and wave amplitude ($Ae^{\beta z}$) are measured directly from the lidar data. For each wave, the observed period $T_{ob} = \lambda_z/c_z$ was calculated from the measured values of λ_z and c_z . The horizontal wavelength ($\lambda_x = \lambda_z T_{ob}/T_B$, where T_B is the buoyancy period) was inferred using the polarization relation for low frequency gravity waves. The measured parameters of each gravity-wave event identified during the 13 observation nights are summarized in Table 2.

The measured vertical wavelengths ranged from 2 to 11.5 km. The maximum vertical wavelength that can be measured is limited by the altitude range of observations, while the minimum value is a function of system noise. Vertical wavelength is plotted versus observation date in Figure 6. No distinct seasonal variations are evident. Dominant wave activity appears to occur at vertical wavelengths near 2-4 km and 7-10 km. The theoretical work of Smith et al. [1987] suggests that the dominant vertical wavelength at stratospheric heights is approximately 5 km. The altitude of maximum wind amplitude associated with 2-4 km vertical wavelength events is predicted to be between 40-60 km [Midgley and Leimohn, 1966]. Because wave events are most likely to be observed at altitudes where the wave amplitude is maximum, our data appear to be consistent with Midgley and Leimohn's predictions.

The values of λ_z observed in this study correspond well with previous radar and lidar measurements. Rayleigh lidar studies with an XeF laser in the 30-65 km altitude range

over Fukuoka, Japan, indicate a dominant vertical wavelength near 10 km [Shibata et al., 1986b]. Rayleigh lidar observations in the same altitude region over Haute Provence Observatory in France show dominant vertical wavelengths on the order of 8-15 km [Chanin and Hauchecorne, 1981]. Sodium lidar studies of the mesopause region (85-105 km) above Urbana also show vertical wavelengths in the 2-15 km range [Gardner and Voelz, 1987]. Radar measurements of λ_z in the 60-110 km altitude region at Saskatoon varied from 0.1-40 km with a median value of 10-15 km [Meek et al., 1985; Manson and Meek, 1988].

Seasonal variations in vertical phase velocity are shown in Figure 7. The vertical phase velocities ranged from 0.11 m/s to 0.85 m/s with a mean value of 0.39 m/s. Shibata et al. [1986b] found vertical phase velocities ranging up to 0.33 m/s with minimums near zero in January and February. This particular trend is not seen in our data. Chanin and Hauchecorne [1981] reported that c_z is a function of altitude with measured values near 1 m/s at 50-70 km and less than 0.2 m/s below 50 km altitude. Vertical phase velocities for gravity waves in the sodium layer (85-105 km) ranged from 0.36 to 1.75 m/s [Gardner and Voelz, 1987].

The observed period of each gravity wave event was inferred from measurements of the vertical wavelength and vertical phase velocity. Values of observed wave periods ranged from 100 to 1000 minutes with a mean value of 240 minutes. The lower value is limited by the 60-minute integration time associated with the individual profiles. Due to the presence of background wind fields, the observed frequency of the wave is the Doppler-shifted frequency rather than the intrinsic frequency. For lidar measurements, the observed periods will be biased to values larger than the corresponding intrinsic wave periods [Gardner and Voelz, 1987]. The seasonal distribution of T_{ob} is shown in Figure 8. Gardner and Voelz did not observe wave events in the sodium layer with periods greater than 200 minutes in summer. The wave periods of the few summer events seen in the data presented here exceed 200 minutes. However, there does appear to be a slight trend

towards shorter periods in summer. The radar technique used by Meek et al. [1985] for mesospheric observations enabled measurements of background winds and the direction of wave propagation. These data were used to compute Doppler shifts of the wave and to estimate the intrinsic period T . Wave periods measured by Meek et al. [1985] varied between 5 and 500 minutes while intrinsic periods were as long as 900 minutes. The more recent radar data reported by Manson and Meek [1988] suggest that the wave periods are shortest in summer which is consistent with lidar data reported here and with the results of Gardner and Voelz [1987]. The Manson and Meek data show that in summer and autumn the majority of the wave periods are shorter than 40 min while in winter the most frequent periods are in the 20 to 60 min range.

For low-frequency gravity waves, the horizontal wavelength associated with a given vertical wavelength and wave period is calculated by applying the dispersion relation. The inferred horizontal wavelengths ranged from 40 km to nearly 2000 km. Seasonal variations in horizontal wavelengths are shown in Figure 9. Because the observed periods, rather than intrinsic periods, were used to calculate the horizontal wavelengths, these results may contain substantial errors and should be used with caution. It should also be emphasized that in computing the horizontal wavelength, the dispersion relation for an isothermal atmosphere was used. In the region between 30 to 50 km, the Brunt-Väisälä period may increase significantly, thus introducing additional uncertainties in the computed horizontal wavelength. Sodium lidar studies did not observe wave events with horizontal wavelengths greater than 400 km in summer [Gardner and Voelz, 1987]. However, no seasonal trends are evident in the data presented here, and the horizontal wavelengths of the few summer events seen in this data set exceed 400 km. The radar data of Meek et al. [1985], Reid and Vincent [1987], and Manson and Meek [1988] show horizontal wavelengths between about 20 and 300 km. Manson and Meek [1988] observed very few long wavelength waves (>400 km) in summer.

The amplitude of each wave event at the mid-point altitude of the observation range is determined by measuring the energy density at the spectral peak and using Eq. (21) to solve for $Ae^{\beta z_c}$. The seasonal distribution of wave amplitudes is illustrated in Figure 9. Most of the calculated wave amplitudes ranged from 1 to 5%. These values correspond to horizontal wind velocities of between 5 and 25 m/s. These values are consistent with radar observations at higher altitudes [Reid and Vincent, 1987; Manson and Meek, 1988]. The amplitudes of monochromatic waves measured near the mesopause with sodium lidar were usually 1 to 5% with maximum values ranging up to 18% [Gardner and Voelz, 1987].

Atmospheric scale heights were computed for each observation date from the average photocount profile for the evening's observations. The seasonal distribution of atmospheric scale heights is shown in Figure 11. Measured scale heights ranged from 6.5 to 7.6 km with a median value of 7 km. Atmospheric scale heights determined from our data appear to be greater in spring and summer months.

The range of parameters measured in this study is consistent with previous measurements of gravity-wave parameters obtained using a wide variety of observation techniques [e.g., Gardner and Voelz, 1987; Reid and Vincent, 1987; and Manson and Meek, 1988]. Dominant vertical wavelengths near 2-4 km and 7-10 km appear evident from both the relative occurrence of wave events and Fourier analysis of the data. Shibata et al. [1986b] appear to have averaged photocount data over altitude to obtain a 1.5 km range bin resolution, and the data presented by Chanin and Hauchecorne [1981] were smoothed over 3.3 km, precluding observations of short wavelength events. Values of c_z measured in this study appear larger than values typically observed in the same altitude region by the other two Rayleigh lidar studies. No seasonal variations of gravity-wave activity are apparent from the wave parameters reported in this study, with the exception of a possible trend to shorter wave periods in the summer. More observations in the summer months are needed to clarify seasonal activity. Our values of c_z in winter are clearly greater than zero, in contrast to the near zero values reported by Shibata et al. [1986b].

6. RELATIONSHIPS BETWEEN GRAVITY-WAVE PARAMETERS

The vertical phase velocity is plotted versus vertical wavelength in Figure 12. There is considerable scatter in the data presented here. A regression curve of the form $c_z = C\lambda_z^p$ where C is the coefficient and p is the slope has been fitted to the data. Since c_z and λ_z are measured parameters, and consequently, both contain errors, the maximum likelihood (ML) regression algorithm described in Voelz and Gardner [1986] was used to estimate the power-law fit for the data presented in this figure. This method assumes measurement errors in the dependent (c_z) and independent (λ_z) parameters are statistically independent and Gaussian distributed. The ML power-law relation obtained from the data is plotted in Figure 12. For comparison, the power-law relation deduced from the sodium lidar data is also plotted (dashed line) [Gardner and Voelz, 1987]. The correlation between c_z and λ_z is very low (0.14) in our Rayleigh data. Events with wavelengths near 2-3 km generally had 0.3 m/s phase velocities when observed with 60-minute integration periods. Shorter vertical wavelengths (2-3 km) that were observed near the mesopause with sodium lidar were associated with phase velocities near 1 m/s, while the longer wavelength (7-10 km) events corresponded to lower phase velocities. The relationship between λ_z and c_z are considerably different for the sodium and Rayleigh lidar observations. This may be due to the fact that the integration periods were substantially different for the two techniques (i.e., 10 min for sodium lidar and 60 min for Rayleigh lidar). However, neither Chanin and Hauchecorne [1981] nor Shibata et al. [1986b] observed large phase velocities in this lower altitude region with 20-minute integration periods.

Both vertical and horizontal wavelengths show a strong tendency to increase with increasing periods and are plotted versus the observed period for each wave event in Figures 13 and 14. Recall from the discussion of Figure 9 that observed periods rather than intrinsic periods were used to calculate the horizontal wavelengths. The values of λ_x may contain substantial errors so the results should be used with caution. The higher

correlation of the data presented in Figure 14 can be partially attributed to the manner in which λ_z is computed [Gardner and Voelz, 1987]. Sodium lidar studies of monochromatic wave activity also indicate that λ_z and λ_x tend to increase with increasing values of T_{ob} [Gardner and Voelz, 1987]. The power-law curves for the sodium data are plotted as dashed lines in Figures 13 and 14 for comparison. Vertical phase velocity is plotted as a function of the observed wave period in Figure 15.

Kinetic energy per unit mass for each monochromatic wave is calculated at the middle of the observation range using Eq. (21). The estimated kinetic energy is plotted versus the vertical wave number $k_z/2\pi$ in Figure 16. Much of the scatter evident here can be attributed to errors due to shot noise. Although the scatter is significant, the ML power-law estimates from the data suggest a k_z^{-2} dependence of kinetic energy. The measured distribution can be compared with the vertical wave number dependence of kinetic energy predicted by the linear saturation theory [Dewan and Good, 1986]. A monochromatic wave is expected to become saturated when its amplitude growth reaches the point of convective instability. This implies that at saturation the horizontal perturbation velocity is approximately equal to the intrinsic horizontal phase speed of the wave,

$$|v_x|_{sat} \approx c_{ix} = c_x - v_0 = \frac{\lambda_x}{T} = \frac{\lambda_z}{T_B} \quad (27)$$

where v_0 is the mean background wind velocity in the direction of wave propagation, T is the intrinsic period of the wave and T_B is the buoyancy period. The KE distribution predicted by saturation theory is then obtained from Eq. (19),

$$KE_{sat} \propto \frac{\lambda_z^2}{2T_B^2} = \frac{N^2}{2k_z^2} \quad (28)$$

The dashed line in Figure 15 is the predicted distribution of KE_{sat} . It should be noted that although the ML power-law fit to the data suggests a k_z^{-2} dependence of kinetic energy, because of the large scatter of the data (which results in a very low correlation value of 0.027) our data should not be taken as conclusive evidence of wave saturation. Indeed, most of the data points at vertical wavelengths greater than 5 km fall below the dashed KE_{sat} line. By comparison, the distribution of kinetic energies observed in sodium lidar studies near the mesopause followed a k_z^{-3} dependence [Gardner and Voelz, 1987].

The kinetic energy of each wave is plotted as a function of the horizontal wave number $k_x/2\pi$ in Figure 17 and observed frequency f_{ob} in Figure 18. Again, k_x was calculated using the gravity wave dispersive relation and observed period. The power law fits indicate a k_x^{-1} and $f_{ob}^{-1.7}$ dependence. The kinetic energy distributions for the sodium lidar data are shown with dashed lines in Figures 17 and 18 [Gardner and Voelz, 1987].

The correlation coefficients for the Rayleigh data power law relationships were usually less than 0.3. In contrast, sodium lidar measurements showed much higher correlation between the gravity wave parameters with values typically ranging between 0.5 and 0.9 [Gardner and Voelz, 1987]. The significant scatter in our Rayleigh data could be attributed to the quality of the data or simply the absence of dominant relationships between the gravity-wave parameters in the upper stratosphere. Meek et al. [1985] also computed power-law relations for λ_z and λ_x versus T and T_{ob} . A comparison of wave parameter relationships obtained from the Rayleigh lidar data, sodium lidar [Gardner and Voelz, 1987], and radar studies Meek et al. [1985] is shown in Table 3.

The differences between the observed relationships deduced from the radar and lidar techniques may be caused by genuine geophysical differences between the various altitude regions and by the particular measurement biases, resolutions, and accuracies that are inherent in each remote sensing technique. It is debatable whether either the radar, sodium lidar or Rayleigh lidar techniques adequately sample the wave field. The radar and lidar techniques measure very different but equally important characteristics of the

monochromatic wave field and they employ radically different selection criteria to identify the wave events. Both techniques are now making important contributions to the study of wave motions in the upper atmosphere and fortunately, the ranges of the various wave parameters measured by both techniques do overlap. It is now essential for measurements to be made simultaneously with both types of systems at the same location so that the strengths and limitations of each technique can be completely characterized.

7. RMS WIND VELOCITY AND KINETIC ENERGY DENSITY

In addition to studying individual wave events, the Rayleigh lidar data can be used to investigate the mean square wind velocity perturbations as a function of altitude. The height profile of velocity perturbations provides a quantitative measure of gravity wave activity and limiting processes in the atmosphere. A profile of velocity versus altitude can be obtained by scaling the mean-square density perturbations which are calculated at each altitude by computing a time average of $r^2(z,t)$ [Miller et al., 1987]

$$\langle v_x^2(z) \rangle = \left(\frac{\gamma H N}{\gamma - 1} \right)^2 \langle r^2(z) \rangle \approx \left(\frac{\gamma H N}{\gamma - 1} \right)^2 \frac{1}{T_0} \int_{t_0}^{t_0 + T_0} r^2(z,t) dt \quad (29)$$

where T_0 is the duration of observation interval. An altitude profile of rms wind velocities for Urbana observations on 8 March 1984 is plotted in Figure 19. To produce this plot each 60-minute density perturbation profile was first spatially low-pass filtered using a cutoff wavelength of 5 km to reduce shot noise contamination. The mean-square density perturbation over the evening was then computed for each range bin and multiplied by the scaling factor $[\gamma H N / (\gamma - 1)]^2$. The oscillations in the data plotted in Figure 19 result from the presence of a slow moving dominant wave. The range of rms velocities is 1 to 4 m/s. Wave amplitude clearly grows with altitude, but the large oscillations make it difficult to accurately estimate a growth length. The effects due to these long period oscillations can be

partially eliminated by averaging the mean-square wind velocity over more observation dates. The rms wind profile from 35-50 km for eight of the Urbana data sets is presented in Figure 20. Only a portion of the Urbana data can be utilized in this calculation due to differences in observation altitudes. The average velocity perturbations increase with altitude with values near 1.75 m/s at 35 km to 3.5 m/s at 50 km. Since the data were low-pass filtered, only gravity-wave activity corresponding to wavelengths greater than 5 km is included. The average amplitude growth length for this profile of rms wind perturbations is 20.9 km. The velocity amplitudes of gravity waves in an isothermal atmosphere are expected to grow exponentially with height as $e^{z/2H}$, in order to conserve kinetic energy. The theoretical growth length for unattenuated waves in this altitude region is $2H \approx 14$ km. Since the measured growth length for the Rayleigh lidar observations is longer than the theoretical growth length, we can infer that waves propagating in this altitude region are, on the average, subject to effects that limit the amplitude growth with altitude. Amplitude growth lengths ranging from 10-100 km with a mean value of 19 km were measured for monochromatic gravity-wave events observed in the sodium layer [Gardner and Voelz, 1987]. Sodium lidar observations of the rms wind perturbations at Urbana also show an 18 km amplitude growth length [Senft et al., 1987]. The wind velocities plotted in Figure 19 can be extrapolated to a value approaching 20 m/s near 85 km by using the measured amplitude growth length of 20.9 km. Velocity perturbations of 20 m/s are comparable to values obtained from sodium lidar measurements [Gardner and Voelz, 1987; Senft et al., 1987].

Both dissipation and saturation processes will attenuate gravity waves as they propagate upward in the atmosphere. Dissipation processes are independent of wave amplitude, while saturation depends upon wave amplitude. To illustrate that waves observed in this study are propagating upward at attenuated growth rates, we compute the altitude profile of kinetic energy density from mean-square velocity perturbations using the relation

$$KE(z) = \frac{\rho(z)}{2} \langle v_x^2(z) \rangle \quad (30)$$

where the atmospheric density $\rho(z)$ is obtained by referencing the lidar profiles to the standard atmosphere at 35 km. The average kinetic energy density profile computed from eight Urbana observation nights is shown in Figure 21. Kinetic energy clearly decreases with altitude. Decreasing kinetic energy with increasing height indicates that either (1) wave energy is being dissipated as waves propagate upward or (2) waves are propagating upward through vertical gradients in the mean background wind flow [Balsley and Garello, 1985; Vincent and Fritts, 1987]. The scale height for the KE profile plotted in Figure 21 is 18.2 km. Vincent and Fritts [1987] calculated kinetic energy scale heights in the 60-110 km altitude region with a MF radar and obtained values ranging from 8.6 to 16.2 km. The kinetic energy density profile shown in Figure 20 is similar to the KE density profile obtained by Balsley and Garello [1985] with the Poker Flat MST radar. The Poker Flat radar was used to measure the mean-square horizontal wind perturbations (E-W direction) at altitudes below 25 km and above 60 km. The rms winds computed from the MST radar KE profile are approximately 8 m/s at 60 km and 1.4 m/s at 25 km. The rms velocities estimated from the Rayleigh lidar data in the 35-50 km altitude region presented above are within these bounds. The values also agree with those estimated by the model computations of Andrews et al. [1987].

8. CONCLUSIONS

In this paper, we have shown that Rayleigh lidar is an effective technique for exploring the dynamics of the atmosphere at altitudes between 30-50 km. This is the region which is presently inaccessible to radar measurements. The propagation of monochromatic gravity waves can be observed by examining altitude profiles of density perturbations and the vertical wave number spectrum of the density perturbations. The data examined in this

study suggest that substantial gravity-wave activity is present in the upper stratosphere. Thirty-six monochromatic wave events were identified and characterized during 13 nights of observations. Significant features of the data are the dominant vertical wavelengths between 2-4 km and 7-10 km and the tendency for both vertical and horizontal wavelengths to increase with an increasing wave period. The kinetic energy density associated with the wave activity obtained from the data is consistent with the assumption that the gravity-wave amplitudes are being limited either by wave saturation or dissipation effects. The estimated magnitude of the rms wind velocity and kinetic energy agree well with values extrapolated from MST radar data outside this height region as well as values predicted from model computations. It should be mentioned that our analysis has been based on the assumption that the lidar-measured density fluctuations are caused by velocity fluctuations associated with gravity waves. Also the horizontal scales were calculated using the gravity wave dispersive relation and observed wave period rather than the intrinsic period such that the effects of background wind have been neglected. Our results, therefore, should be checked to see if they are consistent with the gravity wave assumption. We have demonstrated, at least qualitatively, that they are consistent.

The quality of the data used in this study is relatively poor in comparison to data which can be obtained with wavelength-optimized Rayleigh lidars using state-of-the-art technology. The temporal and spatial resolutions of the data presented here are inadequate to precisely characterize the entire spectrum of quasi-monochromatic wave behavior. Nevertheless, the data analysis techniques developed in this study and the initial experimental results clearly demonstrate the potential of using Rayleigh lidar for dynamics studies. The results already provide estimates of gravity-wave kinetic energy and wave parameters in the upper stratosphere, a region that is inaccessible to radars.

Acknowledgements: This work was supported in part by grants from the Air Force Geophysics Laboratory and the National Science Foundation.

Table 1
UIUC Rayleigh Lidar System Parameters

Laser	Flashlamp Pumped Dye
Laser Wavelength	589 nm
Pulse Energy	50 mJ
Pulse Rate	7.5 pps
Range Resolution	150 m
Receiver Area	1.2 m ²
Receiver Efficiency	5%

Table 2
Measured Gravity Wave Parameters

Date	Observation Altitudes (km)	Vertical Wavelength (km)	Vertical Phase Velocity (ms ⁻¹)	Observed Period (min)	Amplitude* (%)
15 Jan. 1986	30-42	10.5	0.17	1029	1.4
		6	0.25	400	4.0
		4.3	0.14	494	2.68
		4.3	0.3	239	8.25
25 Jan. 1985	38-48	3.8	0.24	259	2.24
		3.3	0.44	124	3.14
		2.2	0.25	145	1.96
13 Feb. 1984	30-40	2.4	0.4	100	2.25
20 Feb. 1984	33-48	10.5	0.46	380	1.79
		2.7	0.28	161	1.74
		2.3	0.28	137	1.74
		2.9	0.25	194	0.89
		2.2	0.32	114	1.18
29 Feb. 1984	35-50	7.2	0.65	186	3.42
		3.4	0.35	164	1.39
		3.4	0.58	99	1.27
		2.4	0.25	162	1.27
8 Mar. 1984	35-50	6.9	0.23	500	2.43
		2.2	0.27	139	2.26
12 Apr. 1985	35-50	3	0.37	135	1.55
22 Apr. 1986	30-45	7.5	0.48	259	2.68
		3.7	0.58	106	5.59
24 Apr. 1984	35-50	6.4	0.52	205	2.47
	35-47	2.9	0.37	129	3.16
		2.2	0.19	190	4.05
17 Jul. 1984	35-50	9.1	0.64	137	2.62
		2	0.32	104	1.09
13 Aug. 1984	35-50	7.7	0.32	417	2.83
	35-45	2.4	0.25	160	2.08
30 Sept. 1984	35-50	11.5	0.85	225	2.53
		6.1	0.38	268	4.56
		6.1	0.61	165	5.37
		3	0.14	357	2.19
		2.3	0.22	174	2.47
12 Nov. 1984	35-50	5	0.65	128	2.53
	35-45	3.5	0.11	530	3.43

*1 % corresponds to a horizontal wind amplitude of approximately 5 ms⁻¹.

Table 3
Comparison of Rayleigh Lidar, Sodium Lidar and MF Radar Measurements of the
Power Law Relationships Between Gravity Wave Parameters

	Rayleigh Lidar Data ¹	Sodium Lidar Data ²	MF Radar Data ³
Altitude Range:	25-55 km	80-105 km	60-110 km
	$c_z = 0.091(\lambda_z)^{0.92}$	$c_z = 4.09(\lambda_z)^{-0.99}$	
	$\lambda_z = 0.028(T_{ob})^{0.93}$	$\lambda_z = 0.4 (T_{ob})^{0.55}$	$\lambda_z = 172(T)^{-0.73}$
	$\lambda_x = 0.016(T_{ob})^{1.73}$	$\lambda_x = 0.093(T_{ob})^{1.52}$	$\lambda_x = 9(T_{ob})^{0.68}$
			$\lambda_x = 39(T)^{0.24}$
	$c_z = 31.4(T_{ob})^{-0.86}$	$c_z = 10.2(T_{ob})^{-0.54}$	
	$KE = 1.3 \times 10^{-5}(k_z)^{-1.87}$	$KE = 1.1 \times 10^{-9}(k_z)^{-2.95}$	
	$KE = 4.0 \times 10^{-4}(k_z)^{-1.01}$	$KE = 5.3 \times 10^{-4}(k_z)^{-1.05}$	
	$KE = 5.2 \times 10^{-6}(k_z)^{-1.74}$	$KE = 9 \times 10^{-5}(k_z)^{-1.59}$	

¹This paper

²Gardner and Voelz, 1987

³Meek et al., 1985

REFERENCES

- Andrews, D. G., J. R. Holton, and C. B. Leovy, *Middle Atmosphere Dynamics*, Chap. 1, Academic Press, New York, 1987.
- Balsley, B. B., and D. A. Carter, The spectrum of atmospheric velocity fluctuations at 8 and 86 km, *Geophys. Res. Lett.*, 9, 465-468, 1982.
- Balsley, B. B., and R. Garello, The kinetic energy density in the troposphere, stratosphere and mesosphere: A preliminary study using the Poke Flat MST radar in Alaska, *Radio Sci.*, 20, 1355-1361, 1985.
- Cerny, T., and C. F. Sechrist, Jr., Calibration of the Urbana lidar system, *Aeron. Rep.*, No. 94, Aeron. Lab., Univ. IL, Urbana, 1980.
- Chanin, M. L., and A. Hauchecorne, Lidar observation of gravity and tidal waves in the stratosphere and mesosphere, *J. Geophys. Res.*, 86, 9715-9721, 1981.
- Dewan, E. M., and R. E. Good, Saturation and the "universal" spectrum for vertical profiles of horizontal scalar winds in the atmosphere, *J. Geophys. Res.*, 91, 2742-2748, 1986.
- Ebel, A., A. H. Manson, and C. E. Meek, Short period fluctuations of the horizontal wind measured in the upper middle atmosphere and possible relationships to internal gravity waves, *J. Atmos. Terr. Phys.*, 49, 385-401, 1987.
- Fritts, D. C., Gravity wave saturation in the middle atmosphere: A review of theory and observations, *Rev. Geophys.*, 22, 275-308, 1984.
- Gardner, C. S., and J. D. Shelton, Density response of neutral atmosphere layers to gravity wave perturbations, *J. Geophys. Res.*, 90, 1745-1754, 1985.
- Gardner, C. S., and D. G. Voelz, Lidar measurements of gravity wave saturation effects in the sodium layer, *Geophys. Res. Lett.*, 12, 765-768, 1985.
- Gardner, C. S., and D. G. Voelz, Lidar studies of the nighttime sodium layer over Urbana, Illinois 2. Gravity waves, *J. Geophys. Res.*, 92, 4673-4694, 1987.

- Gardner, C. S., D. G. Voelz, C. F. Sechrist, Jr., and A. C. Sigel, Lidar studies of the nighttime sodium layer over Urbana, Illinois 1. Seasonal and nocturnal variations, *J. Geophys. Res.*, 91, 13659-13673, 1986.
- Hauchecorne, A., and M. L. Chanin, Density and temperature profiles obtained by lidar between 35 and 70 km, *Geophys. Res. Lett.*, 7, 565-568, 1980.
- Hines, C. O., Internal atmospheric gravity waves at ionospheric heights, *Can. J. Phys.*, 38, 1441-1481, 1960.
- Manson, A. H., and C. E. Meek, Gravity wave propagation characteristics (60-120 km) as determined by the Saskatoon MF radar (Gravnet) system: 1983-85 at 52°N, 107°W, *J. Atmos. Sci.*, 45, 932-946, 1988.
- Meek, C. E., I. M. Reid, and A. H. Manson, Observations of mesospheric wind velocities 1. Gravity wave horizontal scales and phase velocities from spaced wind observations, *Radio Sci.*, 20-1363-1382, 1985.
- Midgley, J. E., and H. B. Leimohm, Gravity waves in a realistic atmosphere, *J. Geophys. Res.*, 71, 3729-3748, 1986.
- Miller, M. S., C. S. Gardner, and C. H. Liu, Rayleigh lidar observations of gravity wave activity in the stratosphere and lower mesosphere, *EOSL Rep. No. 87-008*, University of Illinois, Urbana, December 1987.
- Philbrick, C. R., D. P. Sipler, G. Davidson, and W. P. Moskowitz, Remote sensing of the structure of the middle atmosphere using lidar, Optical Society Topical Meeting on Laser and Optical Remote Sensing: Instrumentation and Techniques, 18, North Falmouth, MA, Sept. 28-Oct. 1, 1987.
- Reid, I. M., and R. A. Vincent, Measurements of the horizontal scales and phase velocities of short period mesospheric gravity waves at Adelaide, Australia, *J. Atmos. Terr. Phys.*, 49, 1033-1048, 1987.

- Richter, E. S., J. R. Rowlett, C. S. Gardner, and C. F. Sechrist, Jr., Lidar observations of the mesospheric sodium layer at Urbana, Illinois, *J. Atmos. Terr. Phys.*, 43, 327-337, 1981.
- Rowlett, J. R., C. S. Gardner, E. S. Richter, and C. F. Sechrist, Jr., Lidar observations of wave-like structure in the atmospheric sodium layer, *Geophys. Res. Lett.*, 9, 683-686, 1978.
- Senft, D., C. S. Gardner, and C. H. Liu, Na lidar measurements of the seasonal and nocturnal variations of the gravity wave vertical wave number spectra, Int. Conf. Gravity Waves Turb. Mid. Atmosphere, Adelaide, May 20-23, 1987.
- Shelton, J. D., C. S. Gardner, and C. F. Sechrist, Jr., Density response of the mesospheric sodium layer to gravity wave perturbations, *Geophys. Res. Lett.*, 7, 1069-1072, 1980.
- Shibata, T., M. Kobuchi, and M. Maeda, Measurements of density and temperature profiles in the middle atmosphere with a XeF lidar, *Appl. Optics*, 25, 686-688, 1986a.
- Shibata, T., T. Kukuda, and M. Maeda, Density fluctuation in the middle atmosphere over Fukuoka observed by a XeF Rayleigh lidar, *Geophys. Res. Lett.*, 13, 1121-1124, 1986b.
- Smith, S. A., D. C. Fritts, and T. E. VanZandt, Comparison of mesospheric wind spectra with a gravity wave model, *Radio Sci.*, 20, 1331-1338, 1985.
- Smith, S. A., D. C. Fritts, and T. E. VanZandt, Evidence for a saturated spectrum of atmospheric gravity waves, *J. Atmos. Sci.*, 44, 1404-1410, 1987.
- Vincent, R. A., and D. C. Fritts, A climatology of gravity wave motions in the mesopause region at Adelaide, Australia, *J. Atmos. Sci.*, 44, 748-760, 1987.
- Voelz, D. G., and C. S. Gardner, Theoretical and lidar studies of the seasonal and nocturnal variations of the mesospheric sodium layer at Urbana, Illinois, *Rep. EOSL 86-006*, Electro-Optic Systems Lab., Univ. IL, Urbana, December 1986.

APPENDIX : RAYLEIGH LIDAR PERFORMANCE EVALUATION

In this appendix we derive the equations which describe the performance of Rayleigh lidar systems. The critical measure of lidar performance is the spatial and temporal resolution. Signal shot noise contaminates the data and limits resolution. The data processing tradeoffs between integration time, observation range and vertical wavelength resolution are described.

The photocount in a Rayleigh lidar system is proportional to atmospheric density and inversely proportional to the square of the range. The expected Rayleigh photocount in the absence of wave perturbations can be modeled as

$$\langle N(z) \rangle = \frac{z_0^2 N_0}{z^2} \frac{\rho(z)}{\rho(z_0)} = \frac{z_0^2 N_0}{z^2} e^{-(z - z_0)/H} \quad (A1)$$

where $N(z)$ is the measured signal photocount and N_0 is the expected photocount at the lower altitude z_0 . The atmospheric density is estimated from the measured photocount by subtracting the background noise count, range scaling the result and multiplying by an appropriate scaling constant ξ . For convenience we will assume the background noise is negligible so that

$$\rho(z) = \xi z^2 N(z). \quad (A2)$$

By substituting Eq. (A2) into Eq. (23) the measured value of $r(z)$ becomes

$$r(z) = \frac{\xi z^2 N(z)}{\rho_0(z)} - 1. \quad (A3)$$

The discrete Fourier transform of $r(z)$ is given by

$$R(k_z) = \sum_m \left[\frac{\xi(m\Delta z)^2 N(m\Delta z)}{\rho_o(m\Delta z)} - 1 \right] e^{ik_z m \Delta z} \Delta z \quad (A4)$$

where Δz is the receiver range gate width. The expected power spectrum is obtained by averaging the magnitude squared of the discrete Fourier transform,

$$\langle |R(k_z)|^2 \rangle = \sum_m \sum_l \left\langle \left[\frac{\xi(m\Delta z)^2 N(m\Delta z)}{\rho_o(m\Delta z)} - 1 \right] \left[\frac{\xi(l\Delta z)^2 N(l\Delta z)}{\rho_o(l\Delta z)} - 1 \right] \right\rangle e^{ik_z(m-l)\Delta z} \Delta z. \quad (A5)$$

Because $N(m\Delta z)$ is a Poisson process, the photocount fluctuations will introduce shot noise into the calculated values of $|R(k_z)|^2$. Equation (A5) can be simplified by noting

$$\langle N(m\Delta z) N(l\Delta z) \rangle = \begin{cases} \langle N_m \rangle \langle N_l \rangle & l \neq m \\ \langle N_m \rangle^2 + \langle N_m \rangle & l = m \end{cases} \quad (A6)$$

so that

$$\begin{aligned} \langle |R(k_z)|^2 \rangle = & \left| \sum_m \left[\frac{\xi(m\Delta z)^2 \langle N(m\Delta z) \rangle}{\rho_o(m\Delta z)} - 1 \right] e^{ik_z m \Delta z} \Delta z \right|^2 \\ & + \sum_m \frac{\xi^2(m\Delta z)^4 \langle N(m\Delta z) \rangle}{\rho_o^2(m\Delta z)} \Delta z^2. \end{aligned} \quad (A7)$$

The first term in Eq. (A7) is the spectrum of the density perturbations while the second term is the shot noise floor.

The expression for the shot noise floor can be simplified by approximating the summation by an integral,

$$\sum_m \frac{\xi^2 (m\Delta z)^4 \langle N_m \rangle}{\rho_0^2(m\Delta z)} \Delta z^2 \approx \int_{z_0}^{z_0+L} \frac{z^2 \Delta z}{z_0^2 N_0} e^{(z-z_0)/H} dz = \frac{\Delta z H}{N_0} \left(1 + \frac{L-H}{z_0}\right)^2 e^{L/H} \quad (A8)$$

We note that the shot noise level is inversely proportional to the photocount at z_0 and grows exponentially with L , the altitude range of the observations. Equation (A8) clearly shows that the shot noise floor is smaller for observations at lower altitudes and smaller observation ranges. By substituting Eq. (A8) into Eq. (A7) and scaling the result according to Eq. (10) we obtain an expression for the measured gravity wave spectrum

$$\frac{1}{2L} \left(\frac{\gamma H N}{\gamma - 1} \right)^2 \langle |R(k_z)|^2 \rangle \approx E_x(k_z) + \frac{1}{2L} \left(\frac{\gamma H N}{\gamma - 1} \right)^2 \frac{\Delta z H}{N_0} \left(1 + \frac{L-H}{z_0}\right)^2 e^{L/H}. \quad (A9)$$

It is more convenient to express the shot noise floor in terms of the total photocount comprising a profile

$$N_T = \sum_m \langle N(m\Delta z) \rangle \approx \frac{z_0^2 N_0}{\Delta z} \int_{z_0}^{z_0+L} \frac{e^{(z-z_0)/H}}{z^2} dz = \frac{N_0 H}{\Delta z}. \quad (A10)$$

By solving this equation for N_0 and substituting the result into Eq. (A9), the measured gravity wave spectrum becomes

$$\frac{1}{2L} \left(\frac{\gamma H N}{\gamma - 1} \right)^2 \langle |R(k_z)|^2 \rangle \approx E_x(k_z) + \frac{1}{2L} \left(\frac{\gamma H N}{\gamma - 1} \right)^2 \frac{H^2}{N_T} \left(1 + \frac{L-H}{z_0}\right)^2 e^{L/H}. \quad (A11)$$

The theoretical spectrum for saturated gravity waves in the middle atmosphere is [Dewan and Good, 1986; Smith et al., 1987],

$$E_x(k_z) \approx \frac{N^2}{2k_z^3}. \quad (\text{A12})$$

This expression can be used in Eq. (A11) to determine the range of vertical wavelengths where the energy density is greater than the noise floor. The result is

$$\left[\frac{8\pi^3}{LN_T} \left(\frac{\lambda H^2}{\lambda - 1} \right)^2 \left(1 + \frac{L-H}{z_0} \right)^2 e^{L/H} \right]^{1/3} < \lambda_z \quad (\text{A13})$$

Equation (A13) defines the spatial resolution of the Rayleigh lidar. Short wavelengths can be observed by increasing the total photocount N_T or by decreasing the altitude range of observations L . The photocount return is enhanced by increasing the laser power, enlarging the receiver telescope area, or lengthening the measurement integration period.

The equations derived above can now be used to evaluate the expected performance of Rayleigh measurements obtained with the UIUC lidar system. Since L and z_0 are data processing parameters, N_T is the only variable in the above equations that is a function of system operating characteristics. The total signal photocount comprising a profile is computed using Eq. (A10) where N_0 is determined from the Rayleigh lidar equation. The lidar equation gives the expected number of backscattered photocounts from a laser directed into the atmosphere [Cerny and Sechrist, 1980]. The expected Rayleigh photocount per pulse from a scattering volume Δz thick centered at altitude z is given by

$$N(z) = \frac{\lambda E_L}{hc} \eta A_r T_a^2 \frac{\sigma_R n_A(z) \Delta z}{4\pi z^2} \quad (\text{A14})$$

where,

λ = laser operating wavelength (m),

E_L = laser energy per pulse (J),

h = Planck's constant (6.63×10^{-34} J-sec),

c = speed of light (3×10^8 m/sec),

A_R = effective receiver area (m^2),

T_a = one-way atmospheric transmittance (0.05),

σ_R = Rayleigh backscatter cross section (m^2),

$n_A(z)$ = atmospheric number density at altitude z (m^{-3})

Δz = range bin width (m).

The product of the Rayleigh backscatter cross section and atmospheric density can be expressed in terms of atmospheric pressure and temperature [Cerny and Sechrist, 1980]

$$\sigma_R n_A(z) = 3.54 \times 10^{-6} \frac{P(z)}{T(z)} \left(\frac{589}{\lambda(nm)} \right)^{4.0117} \quad (A15)$$

where

$P(z)$ = atmospheric pressure (mbar) at altitude z

$T(z)$ = atmospheric temperature (K) at altitude z

By substituting Eq. (A15) into (A14) and using the system parameters listed in Table 1 we can compute the shot noise floor and vertical wavelength resolution as a function of integration time for the UIUC lidar system.

The performance of the UIUC lidar system was evaluated for observations over the 35-50 km altitude range. The predicted shot noise floor is plotted as a function of integration time in Figure A.1. The noise floor is clearly reduced with increased integration time. The vertical wavelength resolution based upon the model gravity wave spectrum is shown in Figure A.2. The expected spatial resolution with 60-minute measurement periods is almost 2 km.

Figure Captions

Figure 1. Simulated vertical wave number spectrum of a monochromatic gravity wave with $\lambda_z = 7.5$ km, $Ae\beta z = 1\%$, $L = 15$ km and $\beta^{-1} = 14$ km, 20 km and 40 km.

Figure 2. Average vertical wave number spectrum measured during 21:18 to 03:42 LST on 13 August 1984 using the UIUC lidar at Urbana, IL. The altitude range of observations is 35 - 50 km and the vertical resolution is 300 km. The dashed line is the estimated shot noise level.

Figure 3. Spatially filtered density perturbation profiles measured on 13 August 1984 using the UIUC lidar at Urbana, IL. The low-pass filter cutoff wave number was 2×10^{-4} corresponding to a cutoff wavelength of 5 km. The diagonal lines indicate the apparent 0.32 m/s downward phase progression of the 7.7 km wave.

Figure 4. Spatially filtered density perturbation profiles measured on 29 February - 1 March 1984 using the UIUC lidar at Urbana, IL. The low-pass filter cutoff wave number was 5.5×10^{-4} corresponding to a cutoff wavelength of 1.8 km. The diagonal lines indicate the apparent 0.25 m/s downward phase progression of the 2.4 km wave.

Figure 5. Average vertical wave number spectrum measured at Urbana, IL on 20 February, 8 March, 17 July, 13 August, 30 September, and 12 November 1984 using the UIUC lidar. The altitude range of observations is 35 - 50 km with a spatial resolution of 300 m and a temporal resolution of 60 minutes. The dashed line is the estimated shot noise floor.

Figure 6. Seasonal distribution of vertical wavelengths.

Figure 7. Seasonal distribution of vertical phase velocities.

Figure 8. Seasonal distribution of observed wave periods.

Figure 9. Seasonal distribution of horizontal wavelengths. The horizontal wavelengths were calculated using the gravity wave dispersion relation by assuming that the intrinsic wave period was equal to the observed period T_{ob} .

Figure 10. Seasonal distribution of wave amplitudes.

Figure 11. Seasonal distribution of atmospheric scale heights.

Figure 12. Vertical phase velocity versus vertical wavelength. The solid line is the ML power-law fit of the form $c_z = C(\lambda_z)^p$ where p is the slope and C is the coefficient. The power-law fit $c_z = 4.09(\lambda_z)^{-0.99}$ obtained with sodium lidar observations is indicated with a dashed line [Gardner and Voelz, 1987].

Figure 13. Vertical wavelength versus observed wave period. The solid line is the ML power-law fit of the form $\lambda_z = C(T_{ob})^p$ where p is the slope and C is the coefficient. the power-law fit $\lambda_z = 0.4(T_{ob})^{-0.55}$ obtained with sodium lidar observations is indicated with a dashed line.

Figure 14. Horizontal wavelength versus observed wave period. The horizontal wavelengths were calculated using the gravity wave dispersion relation by assuming that the intrinsic wave period was equal to the observed period T_{ob} . The solid line is the ML power-law fit of the form $\lambda_z = C(T_{ob})^p$ where p is the slope and C is the coefficient. The power-law fit $\lambda_z = 0.093(T_{ob})^{1.52}$ obtained with sodium lidar observations is indicated with a dashed line.

Figure 15. Vertical phase velocity versus observed wave period. The solid line is the ML power-law fit of the form $c_z = C(T_{ob})^p$ where p is the slope and C is the coefficient. The power-law fit $c_z = 10.2(T_{ob})^{-0.54}$ obtained with sodium lidar observations is indicated with a dashed line [Gardner and Voelz, 1987].

Figure 16. Kinetic energy versus vertical wave number. The solid line is the ML power-law fit of the form $KE = C(k_z)^p$ where p is the slope and C is the coefficient. The kinetic energy dependence predicted by the linear saturation theory is shown in the dashed line.

Figure 17. Kinetic energy versus horizontal wave number. The horizontal wave number was calculated using the gravity wave dispersion relation by assuming that the intrinsic wave period was equal to the observed period T_{ob} . The solid line is the ML power-law fit of the form $KE = C(k_x)^p$ where p is the slope and C is the coefficient. The power-law fit $KE = 5.3 \times 10^{-4}(k_x)^{-1.05}$ obtained with sodium lidar observations is indicated with a dashed line [Gardner and Voelz, 1987].

Figure 18. Kinetic energy versus observed wave period. The solid line is the ML power-law fit of the form $KE = C(f_{ob})^p$ where p is the slope and C is the coefficient. The power-law fit $KE = 9 \times 10^{-5}(f_{ob})^{-1.59}$ obtained with sodium lidar observations is indicated with a dashed line [Gardner and Voelz, 1987].

Figure 19. Altitude variations of rms wind perturbations for 8 March 1984 Urbana data. Each 60-minute density perturbation profile was spatially low-pass filtered using a cutoff wavelength of 5 km.

Figure 20. Altitude variations of rms wind perturbations averaged over eight Urbana observation nights. Each 60-minute density perturbation profile was spatially low-pass filtered using a cutoff wavelength of 5 km.

Figure 21. Altitude profile of kinetic energy density computed from rms wind perturbation data averaged over eight Urbana observation nights.

Figure A.1. Predicted shot noise floor as a function of integration time for observations over 35 - 50 km altitude range using the UIUC lidar system.

Figure A.2. Predicted vertical wavelength resolution as a function of integration time for observations over 35 - 50 km altitude range using the UIUC lidar system.

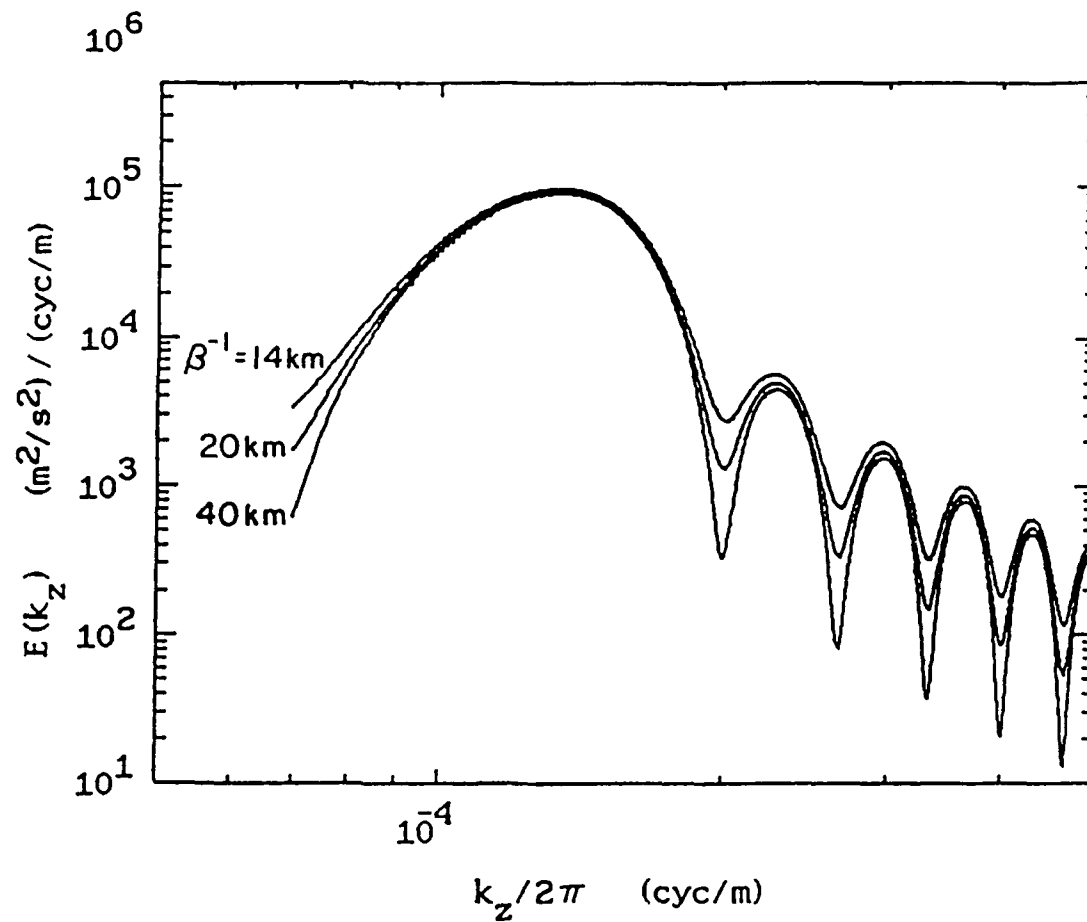


Figure 1. Simulated vertical wave number spectrum of a monochromatic gravity wave with $\lambda_z = 7.5$ km, $Ae^{\beta z} \approx 1\%$, $L = 15$ km and $\beta^{-1} = 14$ km, 20 km and 40 km.

AUGUST 13-14, 1984 21:18-03:42 LST

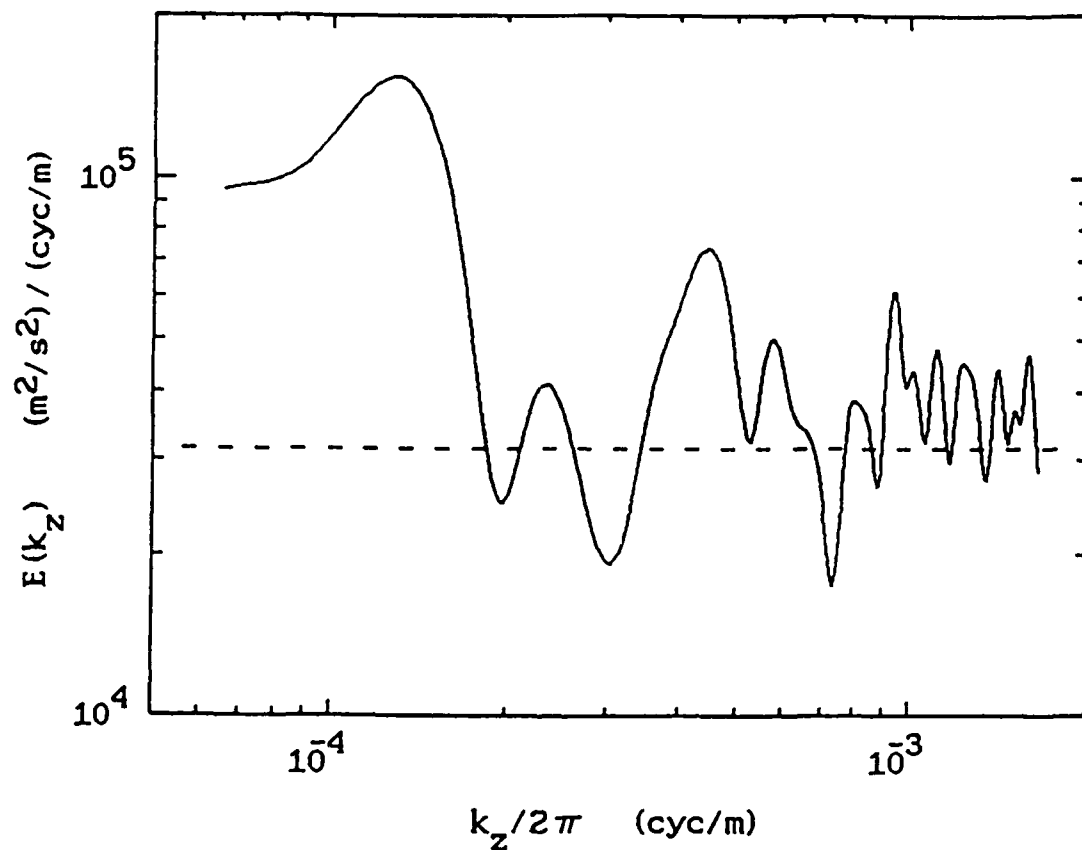


Figure 2. Average vertical wave number spectrum measured during 21:18 to 03:42 LST on 13 August 1984 using the UIUC lidar at Urbana, IL. The altitude range of observations is 35 - 50 km and the vertical resolution is 300 km. The dashed line is the estimated shot noise level.

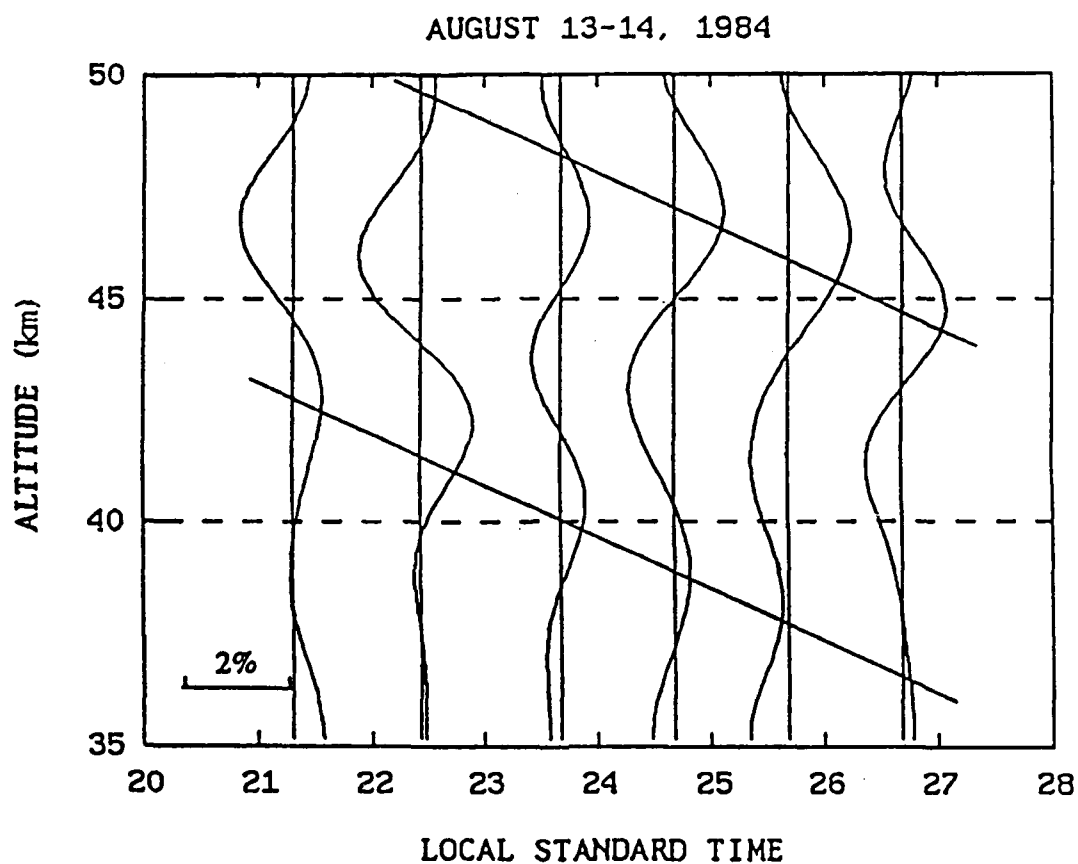


Figure 3. Spatially filtered density perturbation profiles measured on 13 August 1984 using the UIUC lidar at Urbana, IL. The low-pass filter cutoff wave number was 2×10^{-4} corresponding to a cutoff wavelength of 5 km. The diagonal lines indicate the apparent 0.32 m/s downward phase progression of the 7.7 km wave.

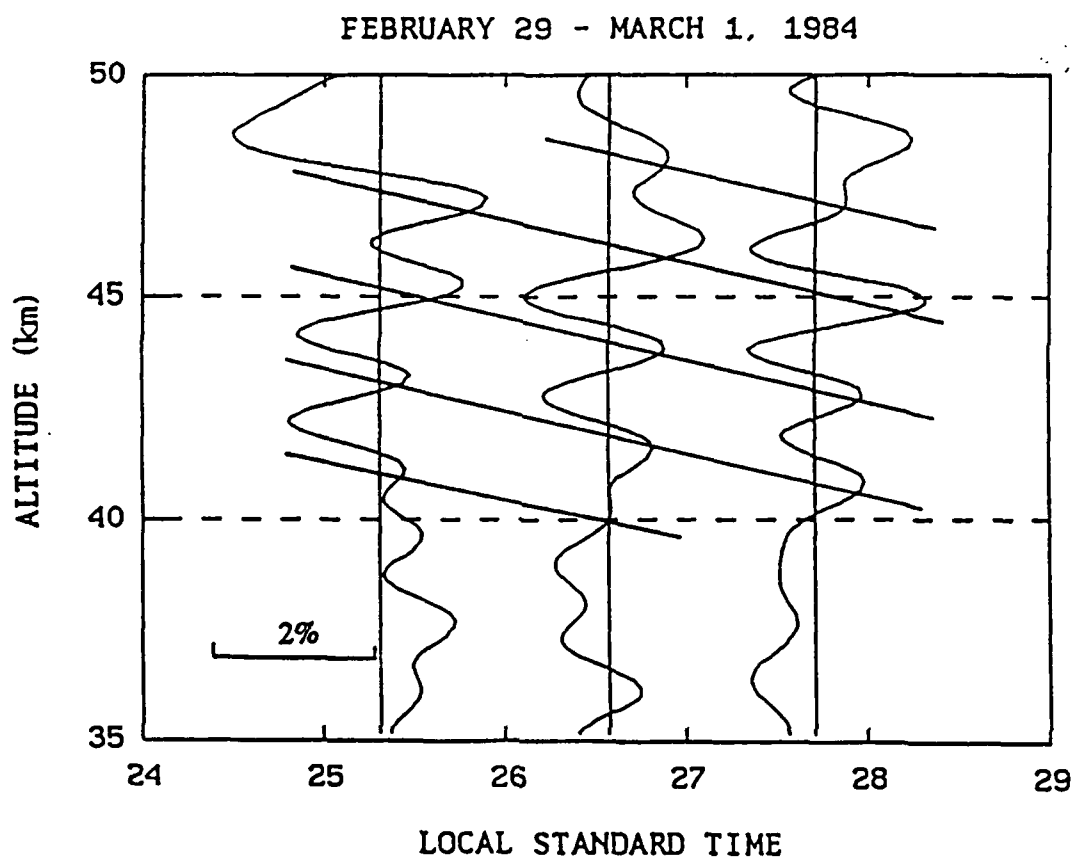


Figure 4. Spatially filtered density perturbation profiles measured on 29 February - 1 March 1984 using the UIUC lidar at Urbana, IL. The low-pass filter cutoff wave number was 5.5×10^{-4} corresponding to a cutoff wavelength of 1.8 km. The diagonal lines indicate the apparent 0.25 m/s downward phase progression of the 2.4 km wave.

URBANA DATA, 1984

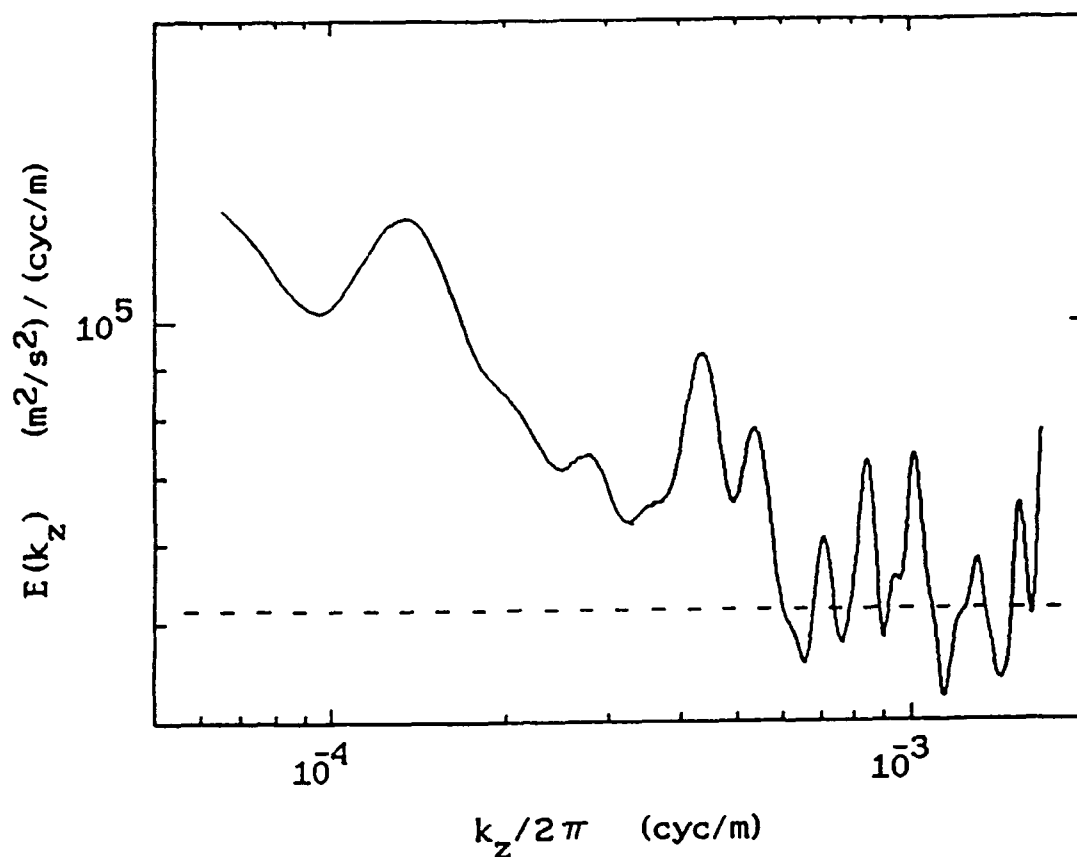


Figure 5. Average vertical wave number spectrum measured at Urbana, IL on 20 February, 8 March, 17 July, 13 August, 30 September, and 12 November 1984 using the UIUC lidar. The altitude range of observations is 35 - 50 km with a spatial resolution of 300 m and a temporal resolution of 60 minutes. The dashed line is the estimated shot noise floor.

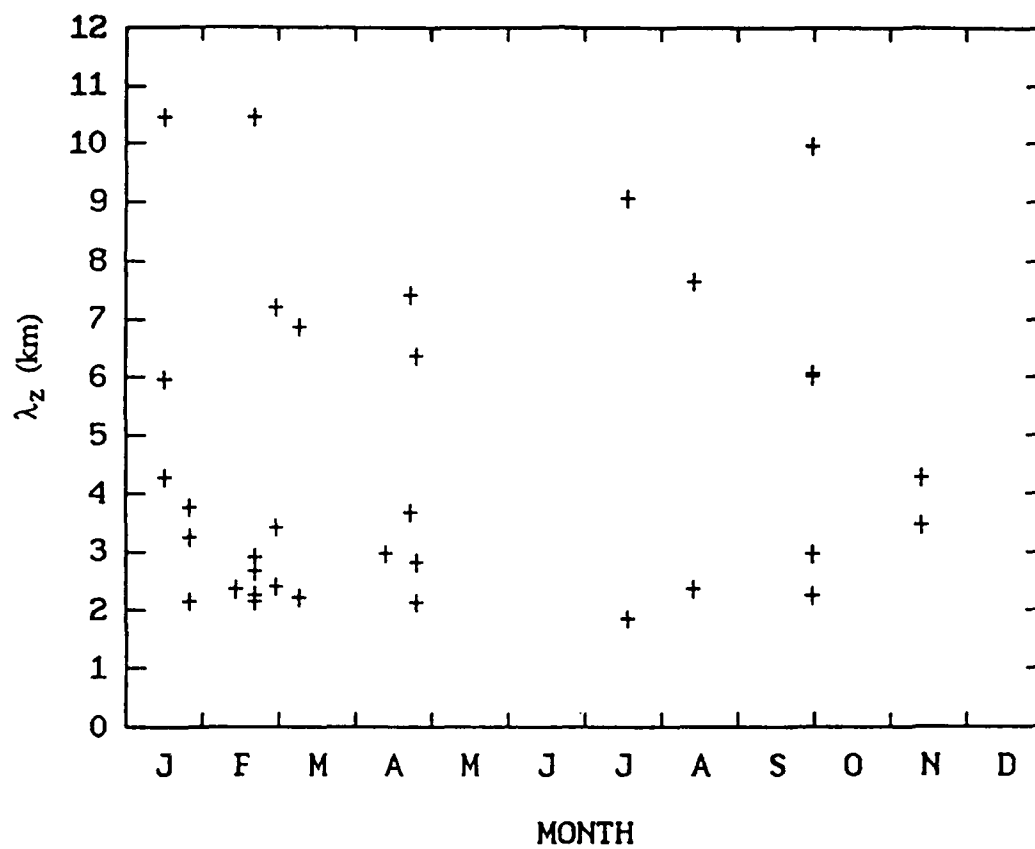


Figure 6. Seasonal distribution of vertical wavelengths.

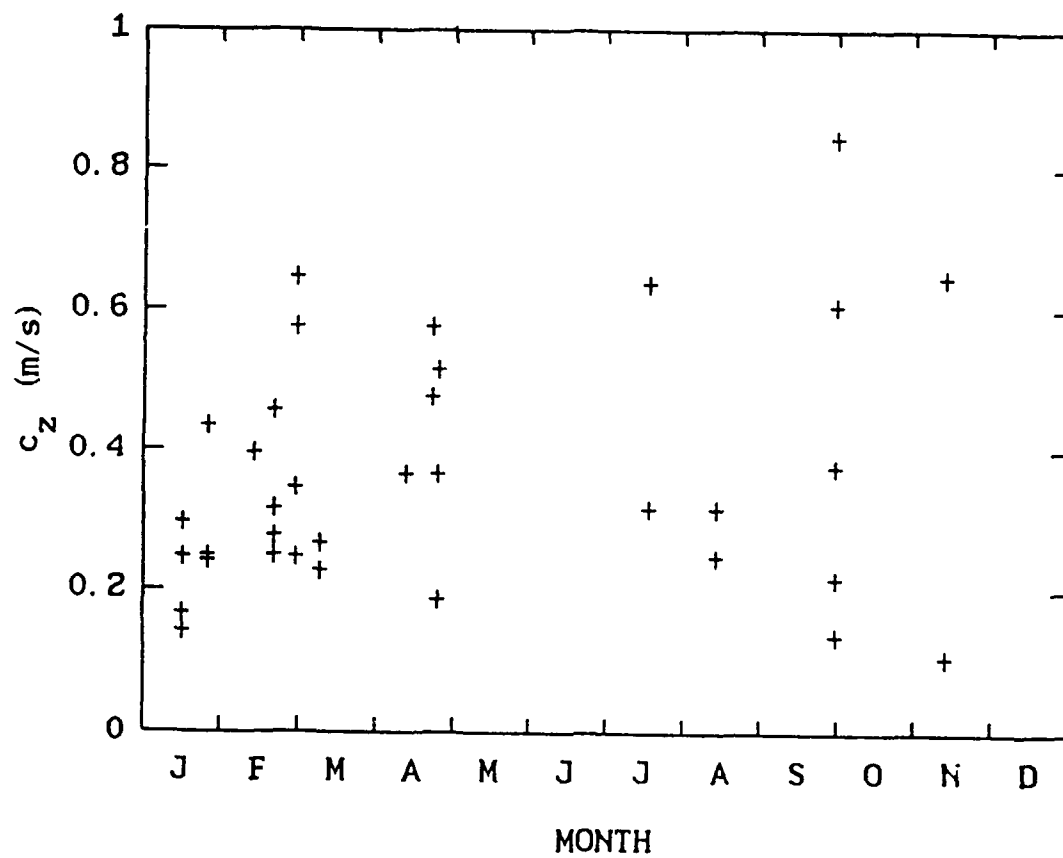


Figure 7. Seasonal distribution of vertical phase velocities.

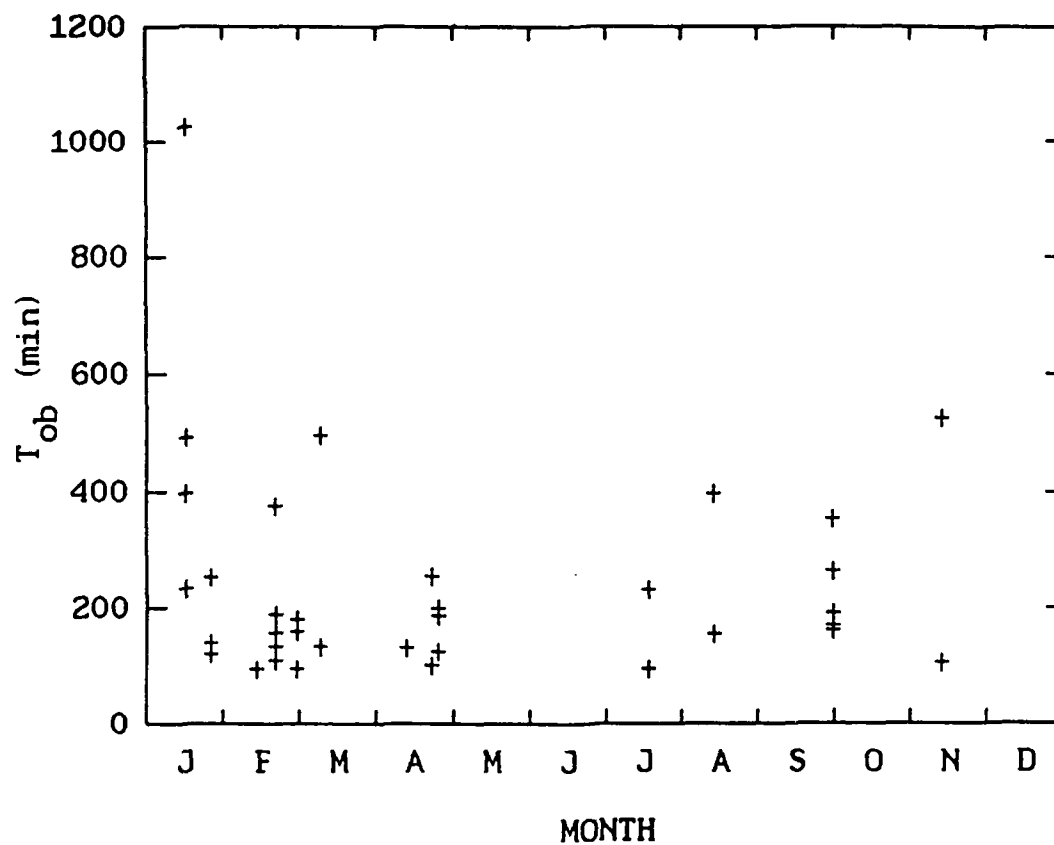


Figure 8. Seasonal distribution of observed wave periods.

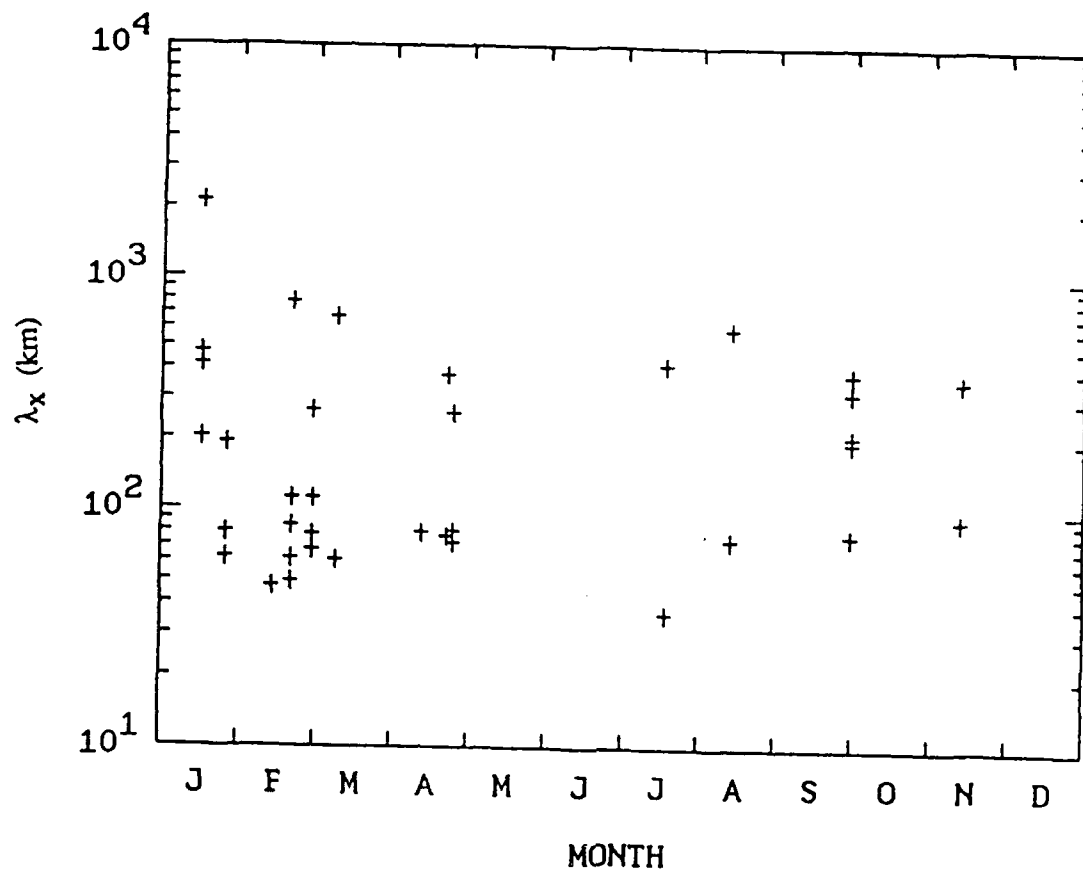


Figure 9. Seasonal distribution of horizontal wavelengths. The horizontal wavelengths were calculated using the gravity wave dispersion relation by assuming that the intrinsic wave period was equal to the observed period T_{ob} .

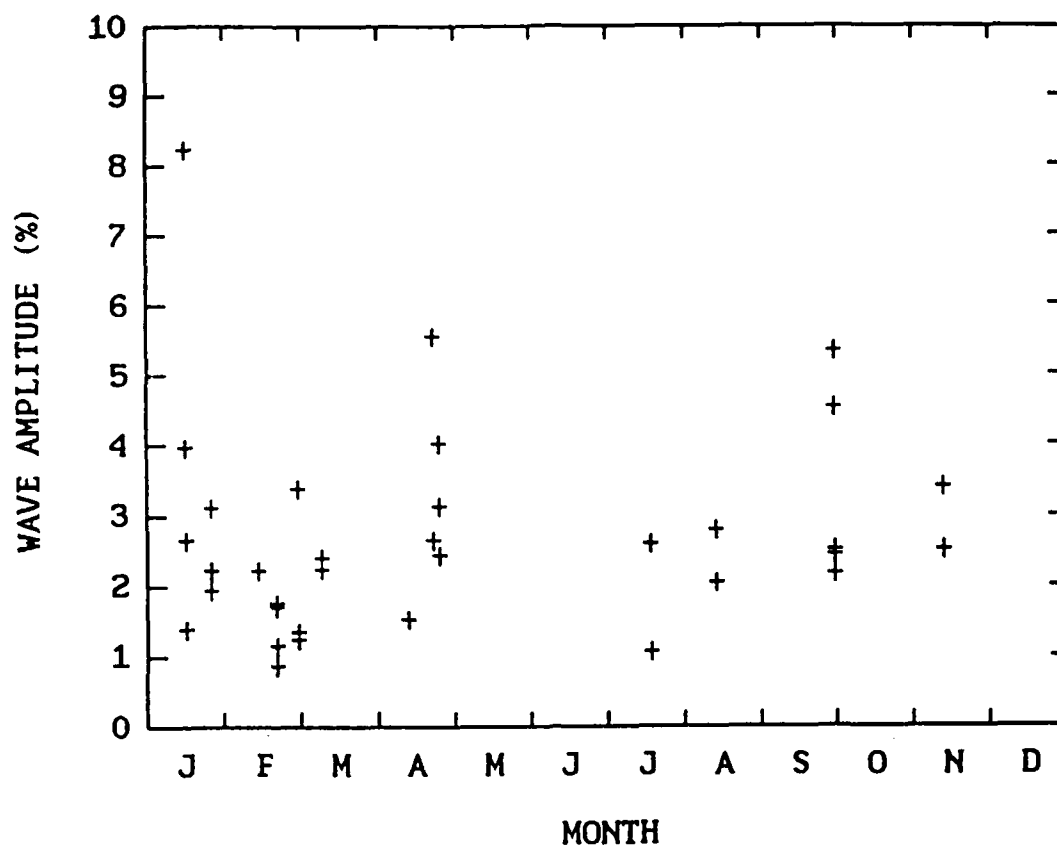


Figure 10. Seasonal distribution of wave amplitudes.

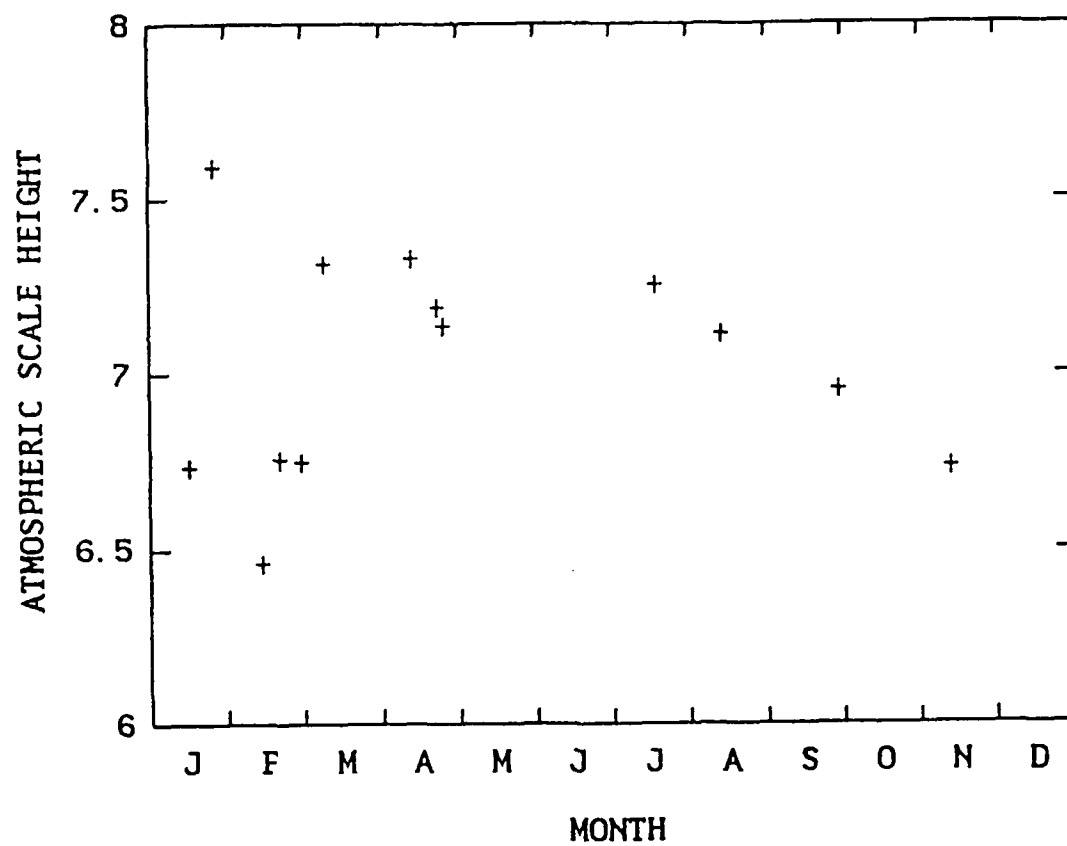


Figure 11. Seasonal distribution of atmospheric scale heights.

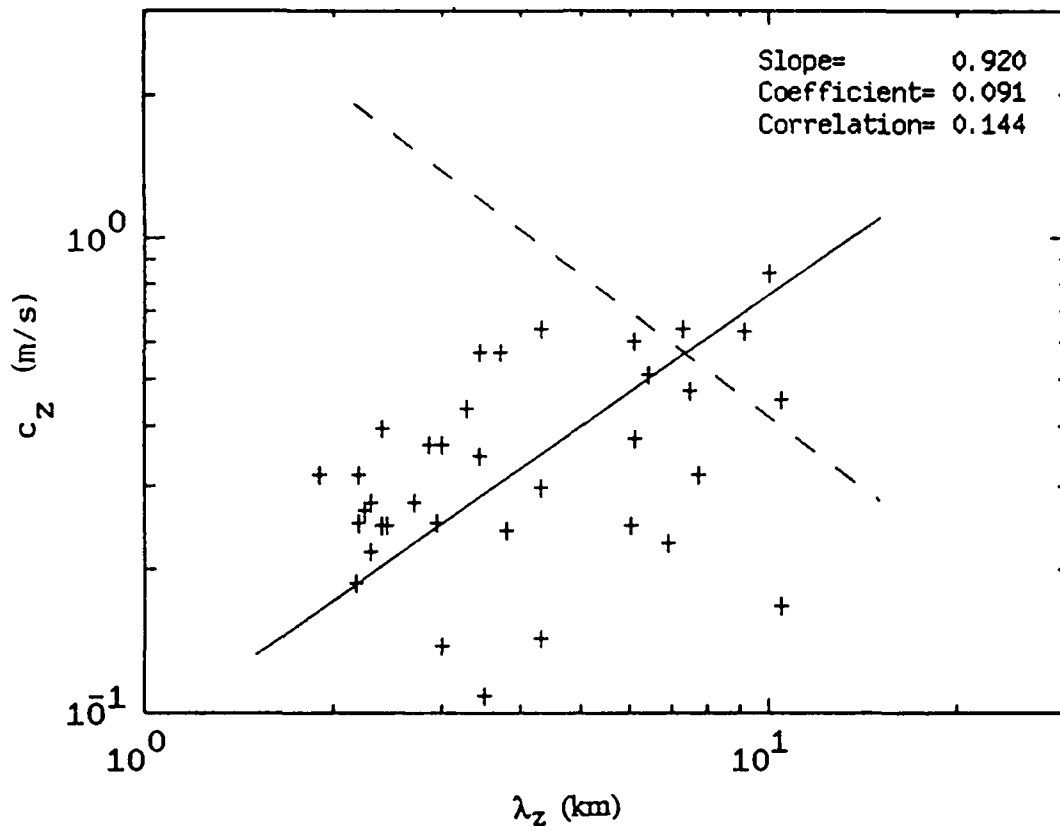


Figure 12. Vertical phase velocity versus vertical wavelength. The solid line is the ML power-law fit of the form $c_z = C(\lambda_z)^p$ where p is the slope and C is the coefficient. The power-law fit $c_z = 4.09(\lambda_z)^{-0.99}$ obtained with sodium lidar observations is indicated with a dashed line [Gardner and Voelz, 1987].

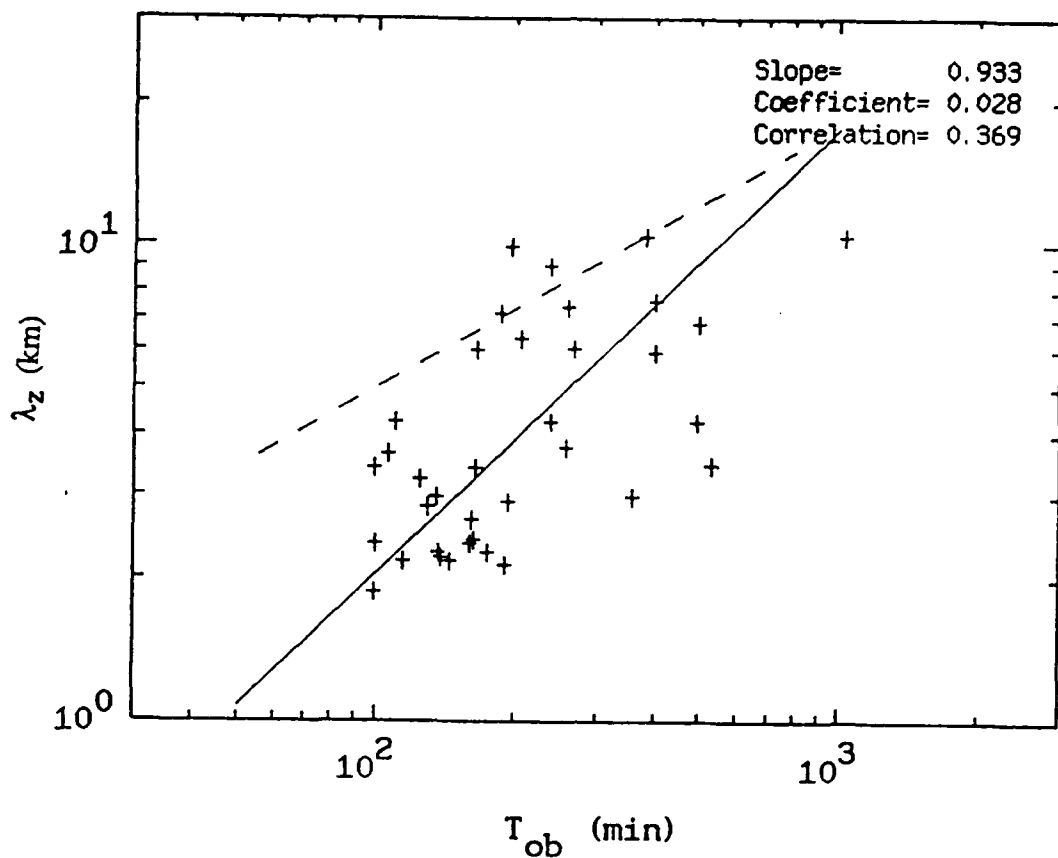


Figure 13. Vertical wavelength versus observed wave period. The solid line is the ML power-law fit of the form $\lambda_z = C(T_{ob})^p$ where p is the slope and C is the coefficient. the power-law fit $\lambda_z = 0.4(T_{ob})^{-0.55}$ obtained with sodium lidar observations is indicated with a dashed line.

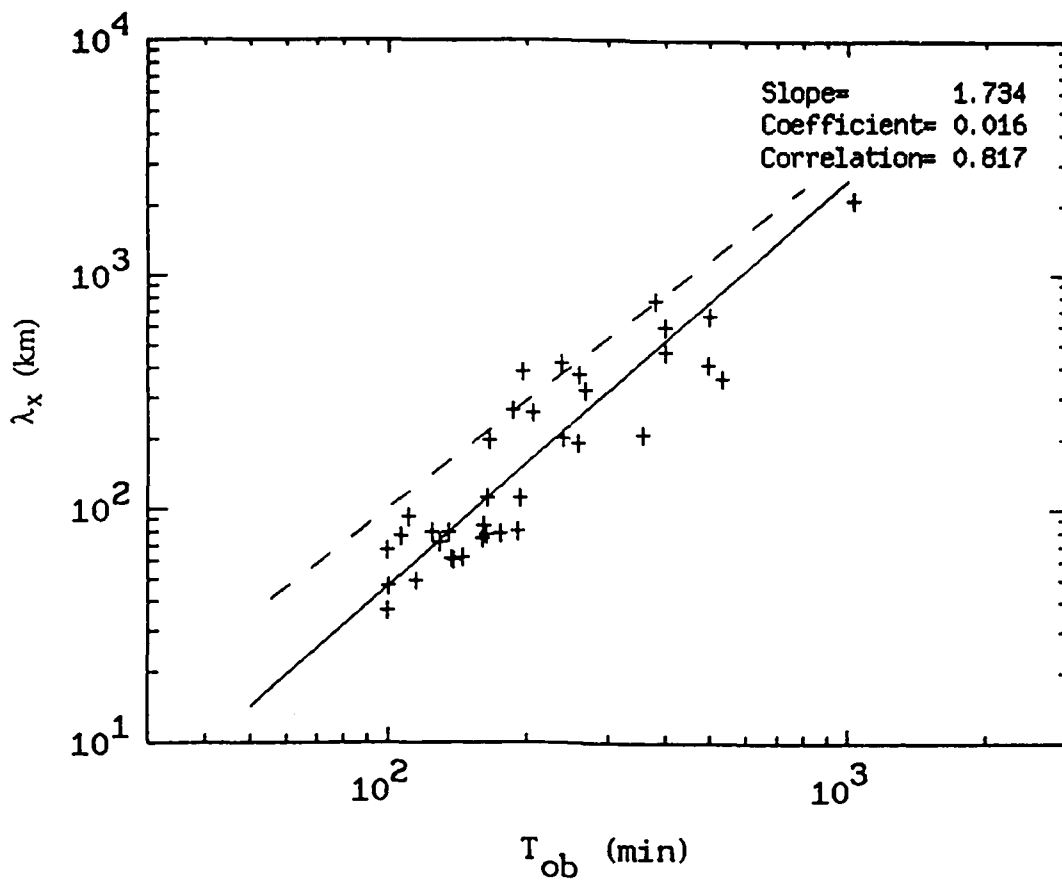


Figure 14. Horizontal wavelength versus observed wave period. The horizontal wavelengths were calculated using the gravity wave dispersion relation by assuming that the intrinsic wave period was equal to the observed period T_{ob} . The solid line is the ML power-law fit of the form $\lambda_z = C(T_{ob})^p$ where p is the slope and C is the coefficient. The power-law fit $\lambda_z = 0.093(T_{ob})^{1.52}$ obtained with sodium lidar observations is indicated with a dashed line.

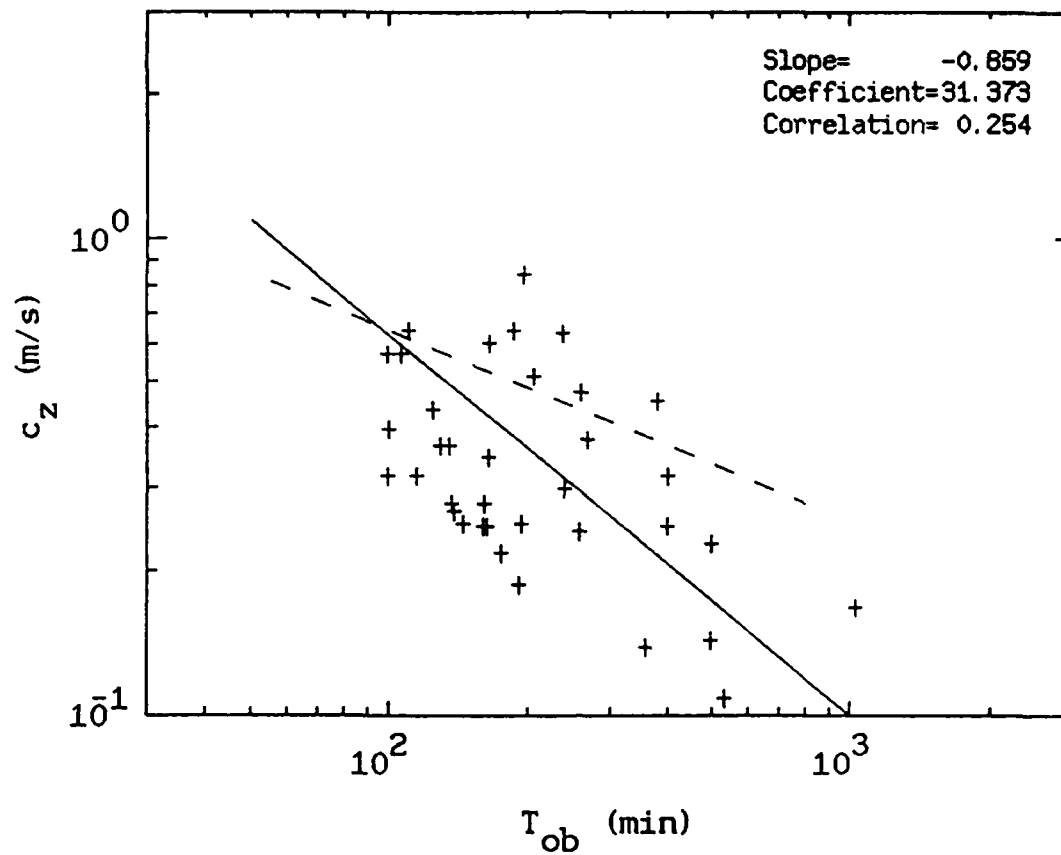


Figure 15. Vertical phase velocity versus observed wave period. The solid line is the ML power-law fit of the form $c_z = C(T_{ob})^p$ where p is the slope and C is the coefficient. The power-law fit $c_z = 10.2(T_{ob})^{-0.54}$ obtained with sodium lidar observations is indicated with a dashed line [Gardner and Voelz, 1987].

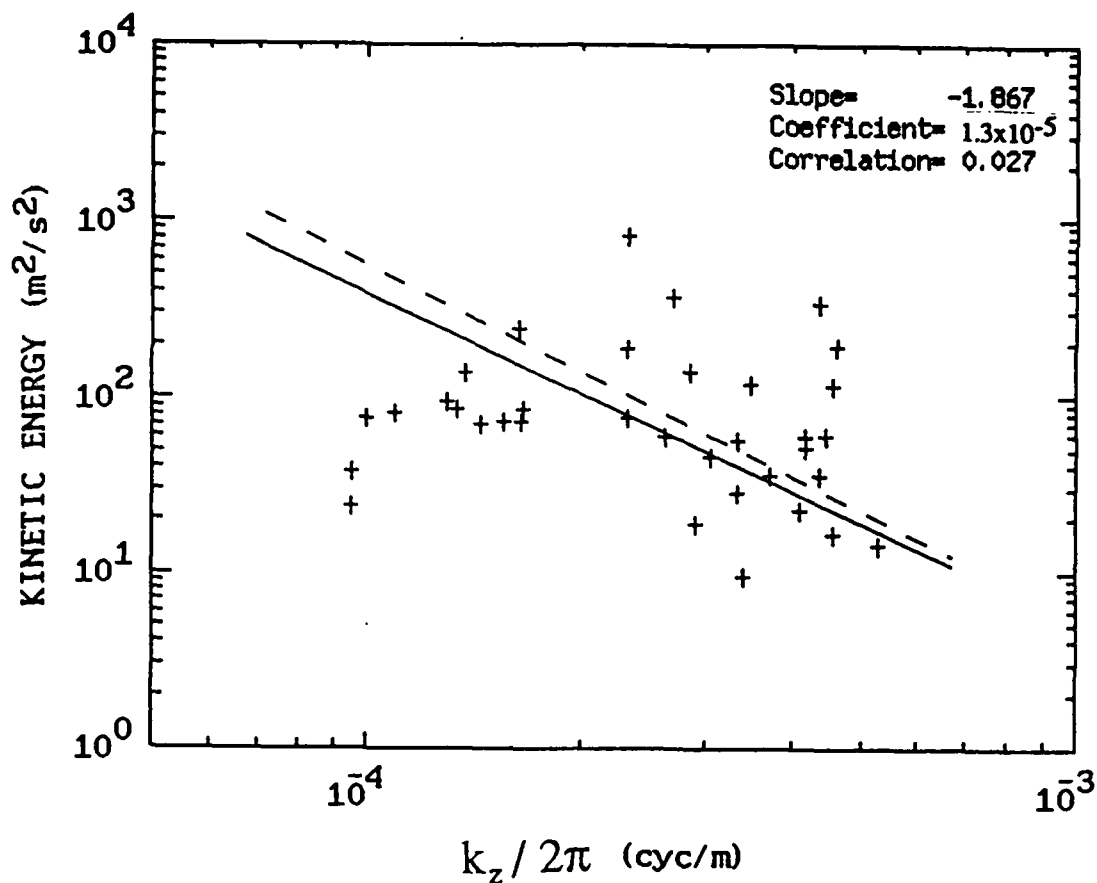


Figure 16. Kinetic energy versus vertical wave number. The solid line is the ML power-law fit of the form $\text{KE} = C(k_z)^p$ where p is the slope and C is the coefficient. The kinetic energy dependence predicted by the linear saturation theory is shown in the dashed line.

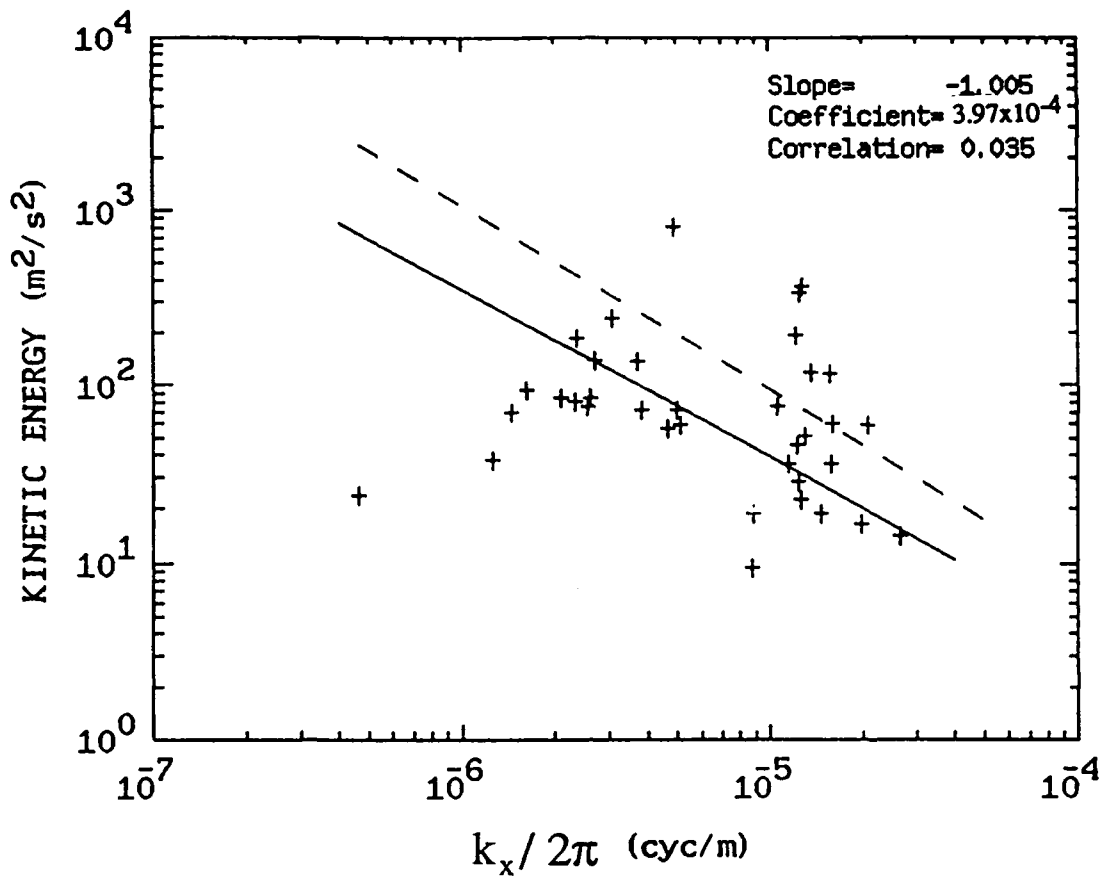


Figure 17. Kinetic energy versus horizontal wave number. The horizontal wave number was calculated using the gravity wave dispersion relation by assuming that the intrinsic wave period was equal to the observed period T_{ob} . The solid line is the ML power-law fit of the form $KE = C(k_x)^p$ where p is the slope and C is the coefficient. The power-law fit $KE = 5.3 \times 10^{-4}(k_x)^{-1.05}$ obtained with sodium lidar observations is indicated with a dashed line [Gardner and Voelz, 1987].

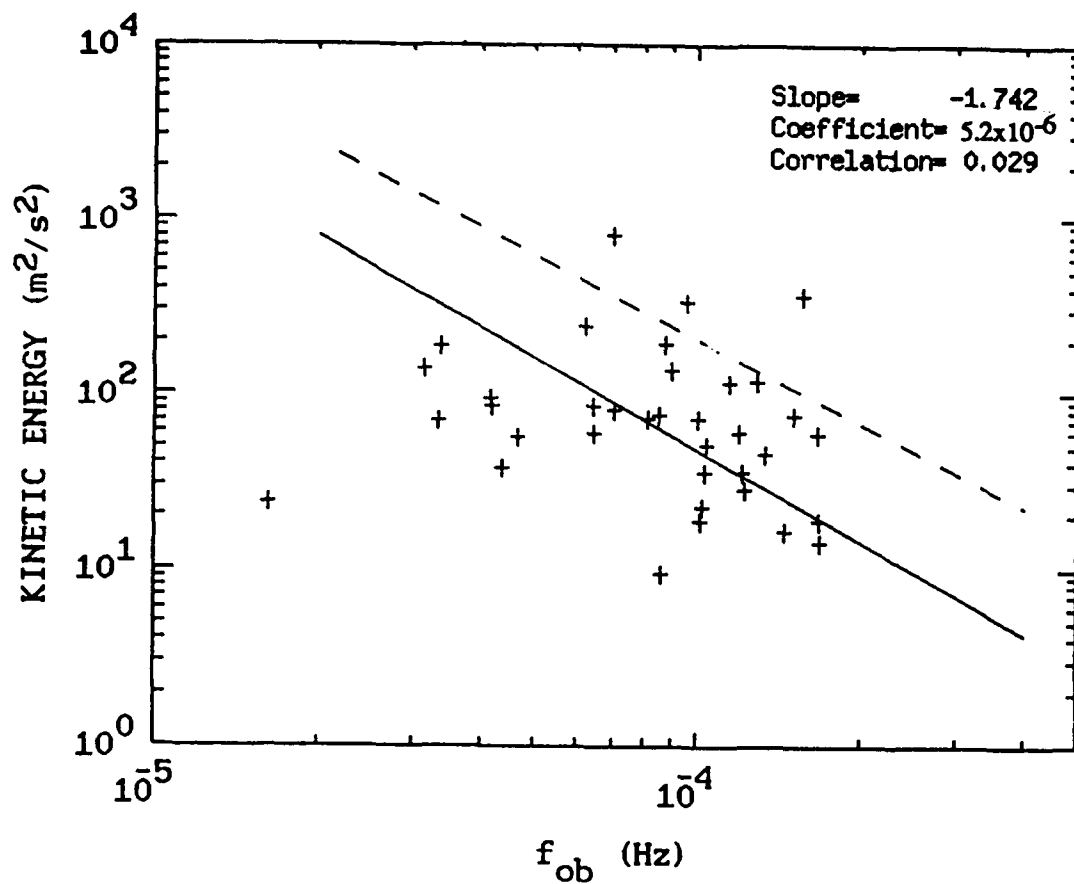


Figure 18. Kinetic energy versus observed wave period. The solid line is the ML power-law fit of the form $KE = C(f_{ob})^p$ where p is the slope and C is the coefficient. The power-law fit $KE = 9 \times 10^{-5}(f_{ob})^{-1.59}$ obtained with sodium lidar observations is indicated with a dashed line [Gardner and Voelz, 1987].

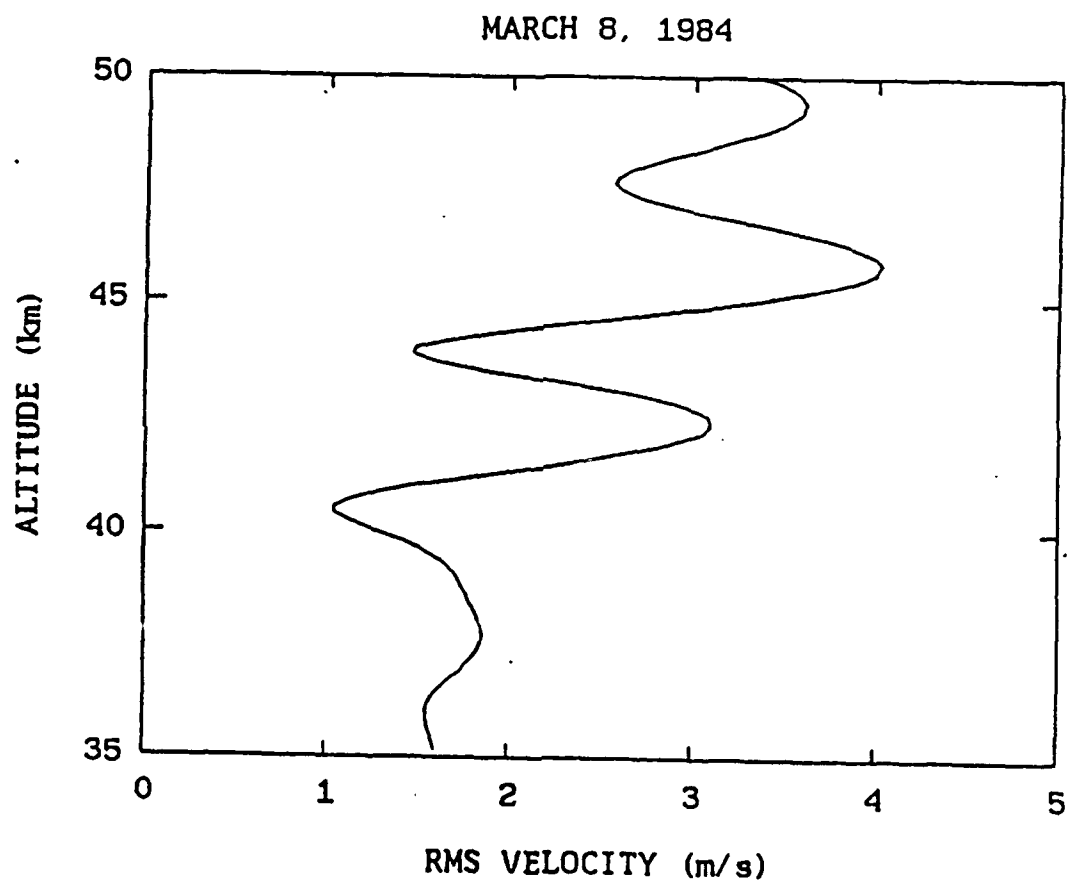


Figure 19. Altitude variations of rms wind perturbations for 8 March 1984 Urbana data. Each 60-minute density perturbation profile was spatially low-pass filtered using a cutoff wavelength of 5 km.

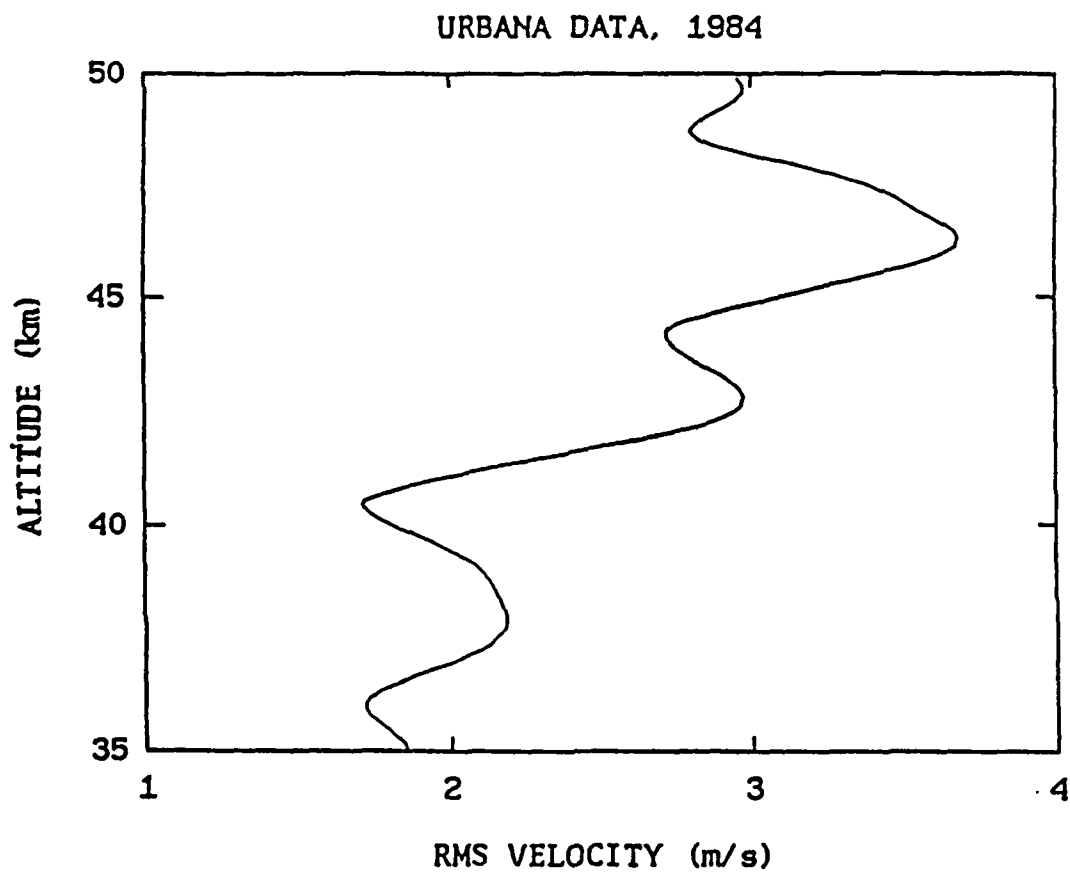


Figure 20. Altitude variations of rms wind perturbations averaged over eight Urbana observation nights. Each 60-minute density perturbation profile was spatially low-pass filtered using a cutoff wavelength of 5 km.

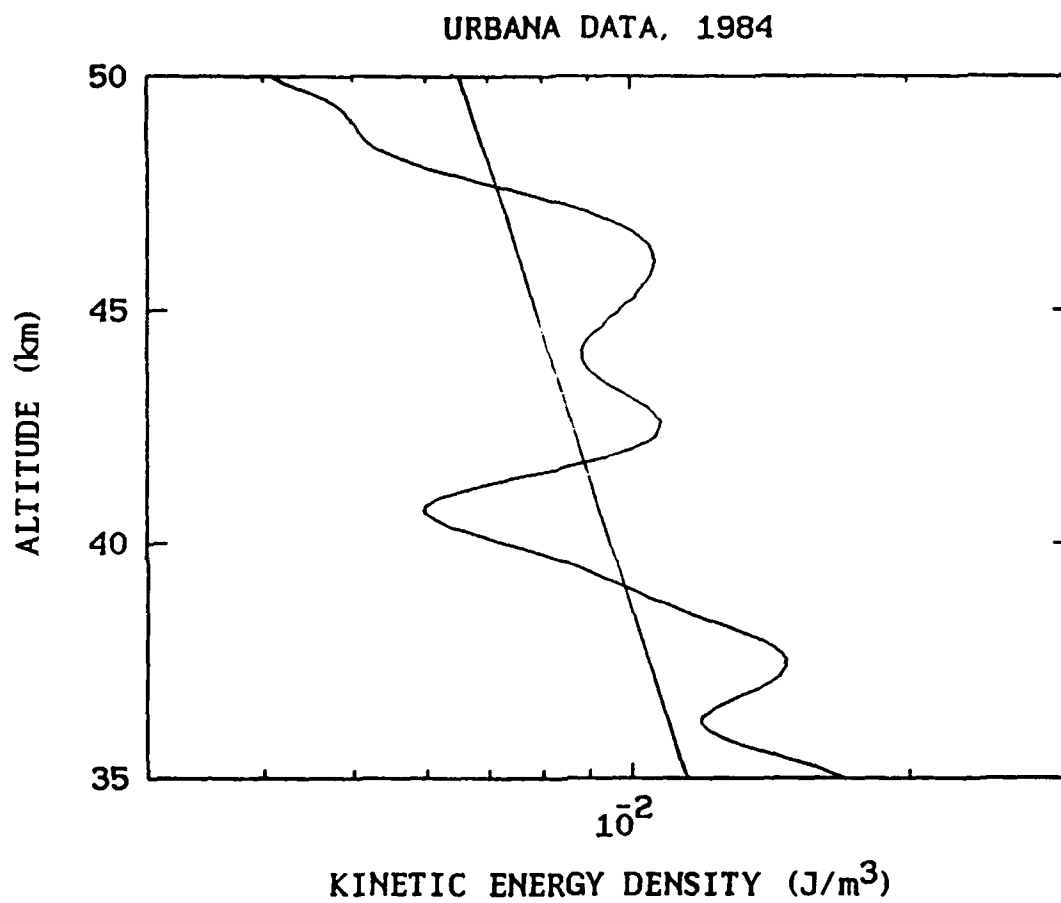


Figure 21. Altitude profile of kinetic energy density computed from rms wind perturbation data averaged over eight Urbana observation nights.

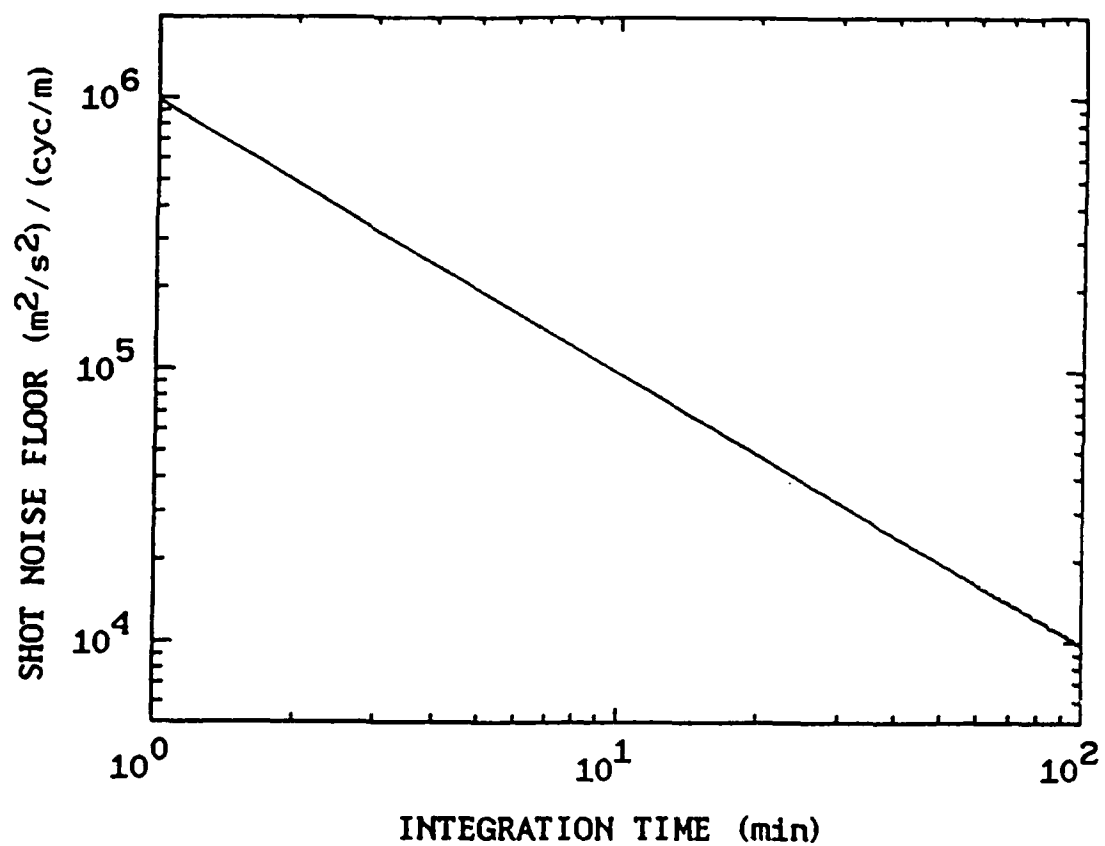


Figure A.1. Predicted shot noise floor as a function of integration time for observations over 35 - 50 km altitude range using the UIUC lidar system.

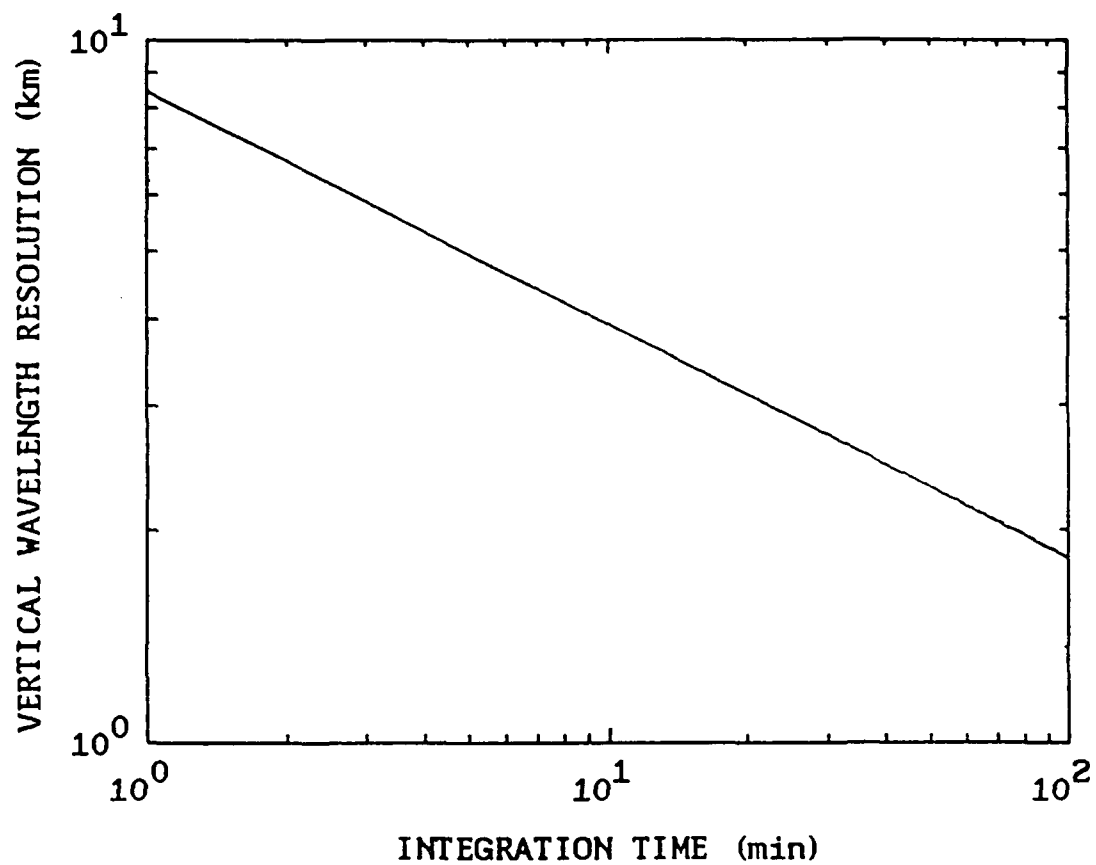


Figure A.2. Predicted vertical wavelength resolution as a function of integration time for observations over 35 - 50 km altitude range using the UIUC lidar system.

END
FILMED

6-89

DTIC